Lithos 175-176 (2013) 104–123

Contents lists available at SciVerse ScienceDirect

Lithos

journal homepage: www.elsevier.com/locate/lithos

SHRIMP U–Pb zircon geochronology and thermal modeling of multilayer granitoid intrusions
Implications for the building and thermal evolution of the Central System batholith, Iberian Massif, Spain

Juan Díaz Alvarado [a], Carlos Fernández [a,*], Antonio Castro [b], Ignacio Moreno-Ventas [b]

[a] Departamento de Geodinámica y Paleontología, Universidad de Huelva, E-21071 Huelva, Spain
[b] Departamento de Geología, Universidad de Huelva, E-21071 Huelva, Spain

ARTICLE INFO

Article history:
Received 21 January 2013
Accepted 9 May 2013
Available online 18 May 2013

Keywords:
Zircon geochronology
Intrusive granitoids
Group mean ages
Sequential emplacement
Thermal rejuvenation

ABSTRACT

This work shows the results of a U–Pb SHRIMP zircon geochronological study of the central part of the Gredos massif (Spanish Central System batholith). The studied batholith is composed of several granodiorite and monzogranite tabular bodies, around 1 km thick each, intruded into partially molten pelitic metasediments. Granodiorites and monzogranites, belonging to three distinct intrusive bodies, and samples of anatectic leucogranites have been selected for SHRIMP U–Pb zircon geochronology. Distinct age groups, separated by up to 20 Ma, have been distinguished in each sample. Important age differences have also been determined among the most representative age groups of the three analyzed granitoid bodies: 312.6 ± 2.8 Ma for the Circo de Gredos Bt-granodiorites (floor intrusive layer), 306.9 ± 1.5 Ma for the Barbellido-Plataforma granitoids (top intrusive layer) and 303.5 ± 2.8 Ma for Las Pozas Crd-monzogranites (middle intrusive layer). These age differences are interpreted in terms of sequential emplacement of the three intrusive bodies, contemporary with the Late Paleozoic D3 deformation phase. The anatectic leucogranites are coeval to slightly younger than the adjacent intrusive granodiorites and monzogranites (305.4 ± 1.6 Ma for Refugio del Rey leucogranites and 303 ± 2 Ma for migmatitic hornfelses). It is suggested that these anatectic magmas were generated in response to the thermal effects of granodiorite intrusions. Thermal modeling with COMSOL Multiphysics® reveals that sequential emplacement was able to keep the thermal conditions of the batholith around the temperature of zircon crystallization in granitic melts (around 750 °C) for several million of years, favoring the partial melting of host rocks and the existence of large magma chambers composed of crystal mush prone to be rejuvenated after new intrusions.

1. Introduction

Traditional ideas about the origin and dynamics of magma chambers and batholith construction have been revised due to new studies (e.g., Coleman et al., 2004; Miller et al., 2011; Paterson et al., 2011). Many batholiths are nowadays considered as examples of composite magma bodies formed by incremental episodes of magma intrusion (e. g., Coleman et al., 2004; Farina et al., 2010). New and accurate zircon geochronological data suggest that magmatic systems could reside in the crust during large periods of time (10^6 years, e.g., Paterson et al., 2011), longer than those obtained by means of thermal modeling of large magmatic bodies (e.g., Walker, 2006 and references therein).

Determinations of strain rates led to proposals that pluton growth is a quick and dynamic process (e.g., Petford et al., 2000). These estimates predict rather short times for pluton growth (less than 10^5 years and strain rates of around 10^{-10} s^{-1}) with independence of the tectonic setting (Fernández and Castro, 1999; Petford et al., 2000). Furthermore, Glazner et al. (2004), based on new geochronological studies and detailed mapping (e.g., the Tuolumne batholith in Sierra Nevada, Coleman et al., 2004), field evidences (laccolith shape of intrusions and co-magmatic contacts), and seismic methods (absence of large magmatic chambers with high melt fractions in active zones) suggested that at least some of the large batholiths are compound, constructed by small increments (sequential magmatic intrusions) over periods of time longer than 10^5 years. This mechanism produces the juxtaposition of magmas with distinct ages and gives rise to complex chemical zoning of plutons (Burgisser and Bergantz, 2011). These new models try to explain a paradoxical observation: homogeneity is the rule at the large scale and heterogeneity at the small scale of large batholiths and their volcanic products.

Incremental growth triggers remobilization of highly viscous crystal-rich mushes belonging to previously intruded granitic batches. Large time gaps, up to several million years, found in

* Corresponding author.

0024-4937/$ – see front matter
http://dx.doi.org/10.1016/j.lithos.2013.05.006

detailed geochronological studies of a single sample apparently support the remobilization hypothesis (Miller et al., 2011). The thermal implications of this process have been widely studied (e.g., Bachmann et al., 2002; Huber et al., 2011). Magmatic recharge can rejuvenate a crystal-rich magma that otherwise could not be able to flow or erupt (Bachmann and Bergantz, 2004). The episodic intrusion of new magma in the magma chamber can increase its volume and pressure up to the point of exceeding the strength of the host rock leading to the eruption of magmatic material. The increase of internal pressure due to new intrusions plays an important role to unlock the crystal framework and to generate significant volumes of volcanic products from partially crystallized magmas (Huber et al., 2010, 2011). These recharge models offer a rheological framework for understanding the association between volcanic activity and emplacement of granitoid magma forming large batholiths (Bachmann and Bergantz, 2004; Burgisser and Bergantz, 2011).

Geochronological studies allow us estimating the residence time of magmas at the emplacement level, adding valuable information to the study of the mechanisms of magma emplacement, and petrological and geochemical evolution of magma chambers in the crust. The acquisition of magmatic fabrics, the geochemical interaction with the host rocks and the ability of magmas to flow and erupt depend on how long this magmatic stage can be maintained. Determination of zircon ages has improved the knowledge of batholith construction by sequential emplacement (Paterson et al., 2008, 2011). Zircon ages are commonly used to date the magma emplacement process. A lively debate is taking place nowadays on how to use zircon data to prove processes such as assimilation (Díaz Alvarado et al., 2011), the nature of magmatic sources (Belousova et al., 2002), the formation of large batholiths (Coleman et al., 2004), or the time intervals involved in crustal recycling (Jeon et al., 2012).

Zircon saturation conditions are used to obtain the temperature of generation and intrusion of granitic magmas (Miller et al., 2003; Watson and Harrison, 1983). This information is essential to assess the thermal evolution of granitoids and host rocks during the sequential formation of batholiths. The experimental study of zircon saturation conditions has allowed understanding the behavior of zircon in granitic melts as a function of magma origin and composition (Watson and Harrison, 1983).

The aim of this paper is to determine the intrusion sequence of the distinct granodiorite bodies that comprise the central part of the Gredos massif (Central System batholith, Iberian Massif). A detailed geochronological study of zircons from 6 samples (4 from intrusive granitoids and 2 from anatectic granites) has been carried out. The ages estimated in the intrusive bodies and anatectic melts shed light on the link between the granodioritic intrusion and the subsequent melt production in the host rocks. Other topics addressed by this work are the analysis of rejuvenation of previously emplaced magma sheets and the characterization of time scales required for building-up the batholith.

2. Geological setting

The Central System batholith (Castro et al., 2002), also called Ávila batholith (Bea et al., 2004), constitutes an almost continuous granite exposure in the Central Iberian Zone of the Iberian Massif (Fig. 1). It represents one of the largest batholiths in the pre-Mesozoic massifs of Western Europe. One of the most salient features of the Central System batholith is the presence of low-P metamorphic complexes that form large roof-pendants completely surrounded by the intruding granodiorites (Fig. 1). These complexes are characterized by the presence of upper crustal migmatites with associated anatectic granites (S-type; according to the original definition of Chappell and White, 1974). Most of these migmatites are derived from pelitic and semipelitic metasediments that form part of the several km thick Neo-Proterozoic turbiditic series (Rodríguez Alonso et al., 2004) and Ordovician ferrosilicic metavolcanics (Fernández et al., 2008, who defined ferrosilicic rocks as those generated from silicic melts with high iron contents, FeO > 4.0 wt.%, for very low calcium contents, CaO < 1.5 wt.%), which are widely represented in the Iberian Massif in Spain and Portugal. The general structure of the Central System batholith in the studied area is that of a layered intrusive complex, with distinct magma batches that successively intruded a migmatitic crust (Yenes et al., 1999). The emplacement of these tabular magma bodies exploited large extensional shear zones affecting the migmatitic host rocks (Díaz Alvarado et al., 2012).

Granitic rocks of granodiorite to monzogranite composition constitute more than 90 vol.% of the intrusive rocks. Minor amounts of more basic rocks ranging from gabbro to Qtz-diorite are present elsewhere in the batholith. Basic rocks represent a mantle input to the source region of the granitoids and radiometric dating indicates that they are mostly coeval or slightly earlier with respect to granodiorite generation (Bea et al., 1999), although later basic intrusions have recently been described (Gutiérrez-Alonso et al., 2011a; Villaseca et al., 2011). In general, all plutonic rocks from gabbros to granodiorites form a typical K-rich calc-alkaline association (Moreno-Ventas et al., 1995) having close similarities with typical Caledonian I-type batholiths (Chappell and Stephens, 1988), and they belong to the large group of intrusives cataloged as “granodiorites” or “calc-alkaline series granitoids” in regional syntheses and classifications of the Paleozoic magmatism of Iberia (Capdevila et al., 1973; Castro et al., 2002).

Geochronological data of the Central System batholith are relatively scarce. The tectono-metamorphic evolution of the northern half of the Central Iberian Zone includes up to four main ductile deformation phases (Table 1 and references therein, Fig. 2): D1 (upright and E-vergent folds, contractional deformation), ~360–337 Ma; D2 (extensional detachments), ~337–316 Ma; and D3 (upright folds and a new extensional episode), ~316–300 Ma. A fourth deformation event (D4) with generation of upright folds and shear bands with normal to oblique displacement has been described for the eastern part of the Iberian Central System (e.g., Rubio Pascual et al., 2013). The metamorphic peak and migmatization of the middle crust in the area occupied by the Central System batholith took place mostly coeval or later than the D2 phase (Table 1). U–Pb and Pb–Pb zircon and monazite geochronology of Variscan granitoids and mafic igneous rocks of the Central System batholith and nearby regions reveals that most of the magmatism is contemporary with the D3 phase (Table 1, Fig. 2). PT determinations in the anatectic complexes of the Central System batholith yielded around 400 MPa and 750 °C for the migmatitic conditions (Pereira, 1993; Pereira and Bea, 1994). More complete analyses have been possible at the Eastern Spanish Central System, where it is preserved an evolution from a first stage attaining up to 1400–1500 MPa and 700–800 °C, followed by an exhumation stage triggered by the D2 extensional phase, with low pressure re-equilibration at 400–700 MPa and associated migmatization (Castiñeiras et al., 2008; Rubio Pascual et al., 2013).

3. Geological features of the studied area

The Gredos massif (Fig. 1) shows good outcrops making it a very interesting place to study the complex kinematic processes associated with the emplacement of large granitic bodies and their evolution with time (Bea et al., 2003; Díaz Alvarado et al., 2012; Montero et al., 2004b). A detailed structural and geochemical study of the central part of the Gredos massif has revealed the presence of three granitoid

Fig. 1. Detailed geological map and cross-section of the studied zone (Gredos massif, Central System batholith, Iberian Massif). Location of the samples used in the geochronological study is indicated in the map. Insets show the outline of the mapped area in a geological sketch of the Spanish Central System and in the Iberian Massif.

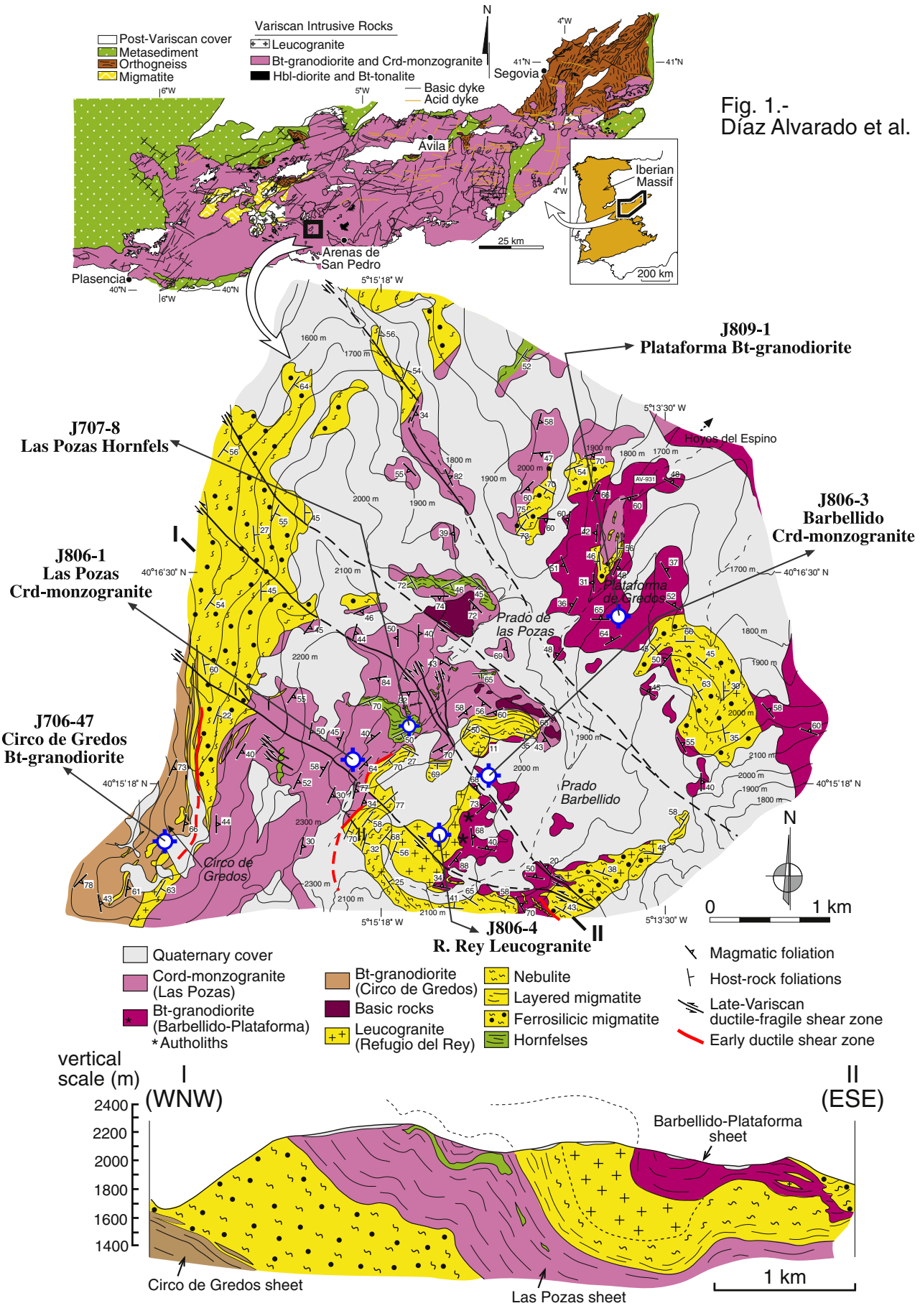

Fig. 1.-
Díaz Alvarado et al.

Table 1
Geochronological data of granitic rocks and main tectono-metamorphic events of the Spanish Central System and nearby regions.

Rocks or tectono-metamorphic event	Geological location	Age (Ma)	Method	Reference
Deformation and metamorphism				
D1 (folds and crustal thickening)	NW Ollo de Sapo Domain	359	$^{40}Ar/^{39}Ar$ whole rock	Dallmeyer et al. (1997)
	Eastern Spanish Central System	>337	U–Pb mnz ID-TIMS	Escuder Viruete et al. (1998)
	Eastern Spanish Central System	354–347	$^{40}Ar/^{39}Ar$ white mica	Rubio Pascual et al. (2013)
D2 (extensional, subhorizontal shear zones)	NW Ollo de Sapo Domain	343	$^{40}Ar/^{39}Ar$ whole rock	Dallmeyer et al. (1997)
	NW Iberia (Sil syncline)	324 ± 7	U–Pb LA-ICP-MS	Martínez Catalán et al. (2004)
	Tormes Dome	325–310	$^{87}Rb/^{87}Sr$ and $^{40}Ar/^{39}Ar$	Escuder Viruete et al. (1994)[a]
	Western Spanisch Central System	332	U–Pb, zrn ID-TIMS	Castiñeiras et al. (2008)[a]
	Eastern Spanish Central System	337–321	U–Pb mnz, ttn ID-TIMS	Escuder Viruete et al. (1998)
	Eastern Spanish Central System	335–316	$^{40}Ar/^{39}Ar$ white mica	Rubio Pascual et al. (2013)
Metamorphic peak	Eastern Spanish Central System	337–326	U–Pb mnz, ttn ID-TIMS	Escuder Viruete et al. (1998)
Migmatization	Eastern Spanish Central System	330	U–Pb zrn SHRIMP	Castiñeiras et al. (2008)
	Spanish Central System (Peña Negra)	350, 332, 313	U–Pb zrn ID-TIMS	Montero et al. (2004b)
	Toledo Massif	317	U–Pb zrn SHRIMP	Castiñeiras et al. (2008)
	Toledo Massif	332	U–Pb zrn SIMS	Bea et al. (2006)
D3 (folds, transcurrent shear zones)	Northern Portugal	320–300	U–Pb zrn, mnz ID-TIMS	Dias et al. (1998)
	Eastern Spanish Central System	316–300	$^{40}Ar/^{39}Ar$ white mica	Rubio Pascual et al. (2013)
Late Paleozoic granitoids and mafic igneous rocks				
Cord leucogranites	Spanish Central System (Peña Negra)	321, 332	U–Pb zrn ID-TIMS	Montero et al. (2004b)
Bt granodiorites and monzogranites	Northern Portugal	319–319	U–Pb mnz, zrn ID-TIMS	Dias et al. (1998)
Granodiorites and monzogranites	Central-Northern Portugal	314–314	U–Pb mnz, zrn ID-TIMS	Valle Aguado et al. (2005)
Granodiorites	Spanish Central System (Peña Negra)	315 ± 6	U–Pb zrn ID-TIMS	Bea et al. (2004)
Bt monzogranites	Northern Portugal	311–306	U–Pb mnz, zrn ID-TIMS	Dias et al. (1998)
"Hot granitoids" and mafic rocks	Central Iberian Zone	311–289	U–Pb zrn LA-ICPMS	Gutiérrez-Alonso et al. (2011a)
"Cold granitoids"	Central Iberian Zone	299 ± 3	U–Pb zrn LA-ICPMS	Gutiérrez-Alonso et al. (2011a)
Granodiorites and monzogranites	Central-Northern Portugal	306 ± 9	U–Pb mnz, zrn ID-TIMS	Valle Aguado et al. (2005)
Bt granite and Crd granite	Spanish Central System (Béjar)	306.6 ± 1.2	U–Pb zrn SHRIMP	Zeck et al. (2007)
Peraluminous leucogranites	Central-Northern Portugal	307.8 ± 0.7	U–Pb mnz, zrn ID-TIMS	Valle Aguado et al. (2005)
Mafic and ultramafic rocks	Spanish Central System (Gredos)	322–307	$^{207}Pb/^{206}Pb$ zrn ID-TIMS	Montero et al. (2004a)
Gabbronorites	Spanish Central System (Béjar)	305.6 ± 1.4	U–Pb zrn SHRIMP	Zeck et al. (2007)
Granites and leucogranites	Eastern Spanish System (La Cabrera)	302 ± 3	$^{207}Pb/^{206}Pb$ zrn ID-TIMS	Casquet et al. (2004)
Two-mica leucogranites	Northern Portugal	300	U–Pb mnz, zrn ID-TIMS	Dias et al. (1998)
"Hot granitoids" and mafic rocks	Northern Spain	297–286	U–Pb zrn LA-ICPMS	Gutiérrez-Alonso et al. (2011a)
"Cold granitoids"	Northern Spain	286 ± 3	U–Pb zrn LA-ICPMS	Gutiérrez-Alonso et al. (2011a)
Bt granites	Northern Portugal	296–290	U–Pb mnz, zrn ID-TIMS	Dias et al. (1998)
Late granite dykes	Eastern Spanish Central System	296 ± 3	$^{87}Rb/^{87}Sr$ whole rock	Galindo et al. (1994)
Camptonitic dyke swarm	Spanish Central System (Gredos)	283 ± 30	$^{87}Rb/^{87}Sr$ whole rock	Bea et al. (1999)

Mineral symbols: mnz, monazite; ttn, titanite; zrn, zircon.
[a] Compilation of previous works.

sheets (Fig. 1), from bottom to top: Circo de Gredos, Las Pozas and Barbellido-Plataforma. The geometry of these bodies is tabular, around 1 km in thickness (Fig. 1, cross section), and intruded along extensional shear zones into a migmatitic crust during the D3 deformation phase of the Variscan Orogeny (e.g., Díaz Alvarado et al., 2012), contemporary to the generation of a huge oroclinal structure (Gutiérrez-Alonso et al., 2011a,b). All of these bodies show K-feldspar megacrysts, mafic microgranular enclaves, and

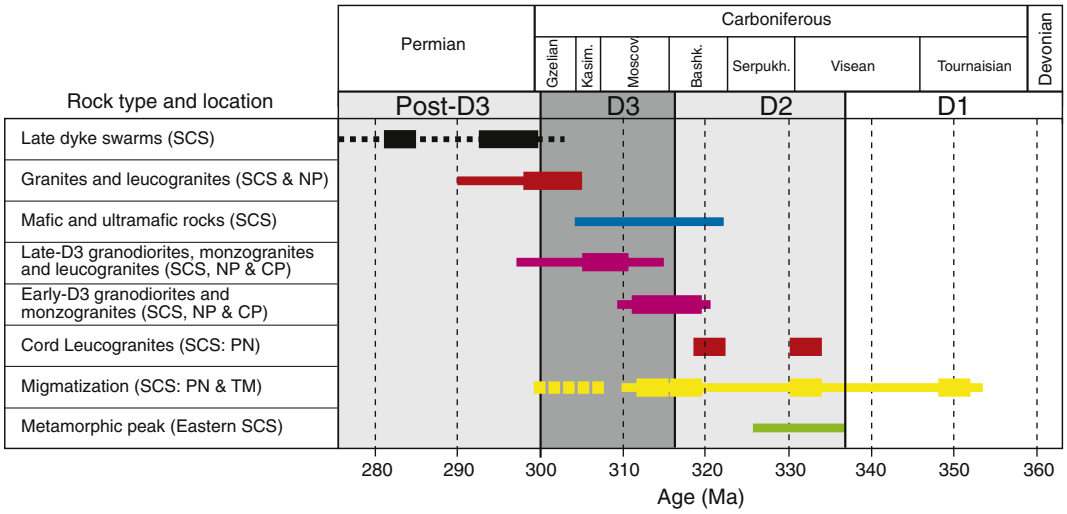

Fig. 2. Diagram showing the age variation and time relations of tectonic and metamorphic processes and granitoid generation and intrusion in the Central System batholith and nearby regions of the Central Iberian Zone (Iberian Massif). See Table 1 for references. The yellow rectangle with vertical pattern corresponds to the migmatization ages determined in this work. SCS: Spanish Central System; NP: Northern Portugal; CP: Central Portugal; PN: Peña Negra; TM: Tormes massif. D1 to D3: Variscan deformation phases described in the main text. (For interpretation of the references to color in this figure legend, the reader is referred to the web version of this article.)

calc-alkaline geochemical signature. However, significant differences can be observed among and inside these bodies at the outcrop and microscopic scales. These differences include variable volume contents of cordierite crystals, inherited zircons and xenoliths, which in some cases have been interpreted as caused by the interaction (including mainly assimilation processes) of magma and host rocks (Díaz Alvarado et al., 2011). Metasedimentary bodies commonly separate the studied granitic sheets, therefore contacts between distinct magmatic batches are rarely observed. Anatectic melts show magma–magma contacts and back-veining relations with the intrusive magmas. These observations suggest that melt generation and segregation in the migmatitic host rocks were coeval with the intrusion of granitic magmas in the study area.

The Circo de Gredos Bt-granodiorite is the lower layer (Fig. 1). This Bt-granodiorite is heterogeneous, showing different facies according to the percentage of Kfs (mineral abbreviations from Kretz, 1983) megacrysts and microgranular enclaves. These facies are organized in large laminar domains. Near the top of this granitic sheet, metasedimentary xenoliths and leucogranite veins are intercalated, and the granodiorite shows euhedral crystals of Crd. The roof contact is a NE–SW directed ductile shear zone (Fig. 3b), moderately dipping to the SE in its current position. Kinematic criteria indicate top-to-the-NE displacement (Díaz Alvarado et al., 2012). The shear zone brings into contact the Circo de Gredos intrusive granitoids (footwall) with an anatectic complex (hanging wall) formed by ferrosilicic migmatites, nebulites and leucogranites with Crd nodules.

The Las Pozas Crd-monzogranite (middle layer) constitutes a tabular body, around 800 m thick, sandwiched between two migmatite layers (Fig. 1). Several septa of migmatite hornfels are included within Las Pozas Crd-monzogranite, particularly near its top. In the vicinity of the contacts with pelitic metasediments, the intrusive granitoid contains abundant xenoliths of partially digested country rocks (Figs. 1 and 3d). Granitoid composition in Las Pozas intrusive body is mainly monzogranitic, although in the central domains, far from the xenoliths and contacts with host rocks, composition is more granodioritic. The percentage of Kfs megacrysts, euhedral Crd and host rock xenoliths are higher than in the Circo de Gredos Bt-granodiorite, increasing the abundance of these components with the proximity to the metasediments (Díaz Alvarado et al., 2011). Ferrosilicic migmatites and nebulites lie beneath the Las Pozas granitoid. This basal limit of the Las Pozas sheet is scarcely deformed and it shows co-magmatic structures like magma–magma contacts. In contrast, the roof contact of Las Pozas Crd-monzogranite sheet is a shear zone (Figs. 1 and 3c). This 15–20 m thick shear zone records a continuous transition from magmatic to solid-state flow (Díaz Alvarado et al., 2012). The shear zone is NE–SO directed, dipping around 60° SE, and it is characterized by the presence of alternating bands, 5–30 cm thick, composed of Crd-monzogranite and migmatite, and arranged parallel to the boundaries of the shear zone (Fig. 3c). The foliation observed inside this shear zone, sub-parallel to their boundaries, is marked by the preferred orientation of the Kfs megacrysts in the Crd-monzogranite, and by the planar arrangement of leucosome, mesosome and melanosome layers in the migmatites. A NE–SW directed mineral and stretching lineation are observed on the previously described foliation. The kinematic criteria described by Díaz Alvarado et al. (2012) indicate a top-to-the-SW displacement for this shear zone. One of the most salient features of Las Pozas intrusive sheet is the presence of large tabular and dismembered bodies of migmatitic hornfels included in monzogranites as large xenoliths or screens. These hornfels xenoliths are composed of two main types of migmatites: phlebite (veined migmatite), which is the dominant variety, and agmatite. These migmatites are characterized by a very small grain size, the presence of Crd in paleosomes and neosomes, and the absence of diagnostic minerals of elevated pressure and temperature (only And is present in some mesosomes). This large body of hornfels xenoliths is appropriate for studying the mechanisms by which crustal fragments are incorporated to the intrusive magmas (Fig. 3d).

The Barbellido-Plataforma intrusive body constitutes the top unit in the study area (Fig. 1). Its thickness is difficult to measure, first because it is wedge-shaped in the studied area (see e.g., cross-section in Fig. 1), and second because its top contact mostly lies outside the mapped area; however a minimum average thickness of 0.5 km must be considered. It consists essentially of Bt-granodiorites with very low volume fraction of Kfs megacrysts (Fig. 3f), except for the contact areas with metasediments, where it is also characterized by the presence of Crd and numerous host rock xenoliths. The Barbellido-Plataforma Bt-granodiorite lies on top of the Refugio del Rey migmatite–leucogranite layer. Magma–magma contacts can be seen between the Refugio del Rey leucogranite and the Barbellido Bt-granodiorite (Fig. 3e).

The granitoid sheets and anatectic complexes show a variably developed magmatic and metamorphic foliation. The structures indicative of solid-state deformation are very rare in the granitic bodies and they can be observed along thin shear bands located inside the main shear zones, which suffered dominant magmatic deformation (Díaz Alvarado et al., 2012). The granitic sheets are syn-tectonic with respect to the activity of large extensional shear zones, as evidenced by the continuity and parallelism between the magmatic fabric of the plutons and the solid-state fabric of the adjacent host rocks, among other criteria (Díaz Alvarado et al., 2012). After the emplacement of the three studied granitic sheets, they were affected by two generations of folds, which originated a complex fold interference pattern (Díaz Alvarado et al., 2012), intermediate between types 1 and 2 of Ramsay (1967). Later, brittle–ductile, sub-vertical, sinistral shear zones, several meter thick and WNW–ESE directed, displaced hundreds of meters the contacts between granite bodies and host-rock (Fig. 1). Dikes of granite porphyry exploited these late shear zones to intrude.

4. Sampling and analytical techniques

4.1. Sampling

Six samples have been selected for the geochronological study (Fig. 1). Four of them correspond to the three layers of granitoids identified in the mapped region. Two samples were selected in the Barbellido-Plataforma granitic body (J806-3 and J809-1) in order to check possible internal age differences in a single sheet and to study the variations in morphology and age of zircons caused by the assimilation process. Two additional samples were taken in the Circo de Gredos (J706-47) and Las Pozas (J806-1) granitic sheets. The two remaining samples correspond to the leucogranites associated with the Refugio del Rey migmatites (J806-4) and the leucosomes of the migmatitic hornfels (J707-8) included in Las Pozas intrusive body. These latter samples were taken to determine the age of generation of leucogranites associated with the anatectic complex and to constrain the time relation of the migmatization process with the intrusion of granitic magmas.

4.2. Zircon preparation and SHRIMP U–Th–Pb analyses

Zircon separation was carried out at the laboratories of the Research Central Services, University of Huelva, using classical procedures including magnetic (Frantz) and density separation. At the Research School of Earth Sciences (Australian National University, Canberra), the non-magnetic, heavy mineral concentration was hand-picked in order to classify and group zircon crystals on the basis of shape, size and lack of fractures or inclusions. The obtained groups were mounted in epoxy resin together with zircon standards SL13 (U = 238) and TEMORA ($^{206}Pb/^{238}U = 0.06683$). The same procedure was carried out for the sample J809-1, which was

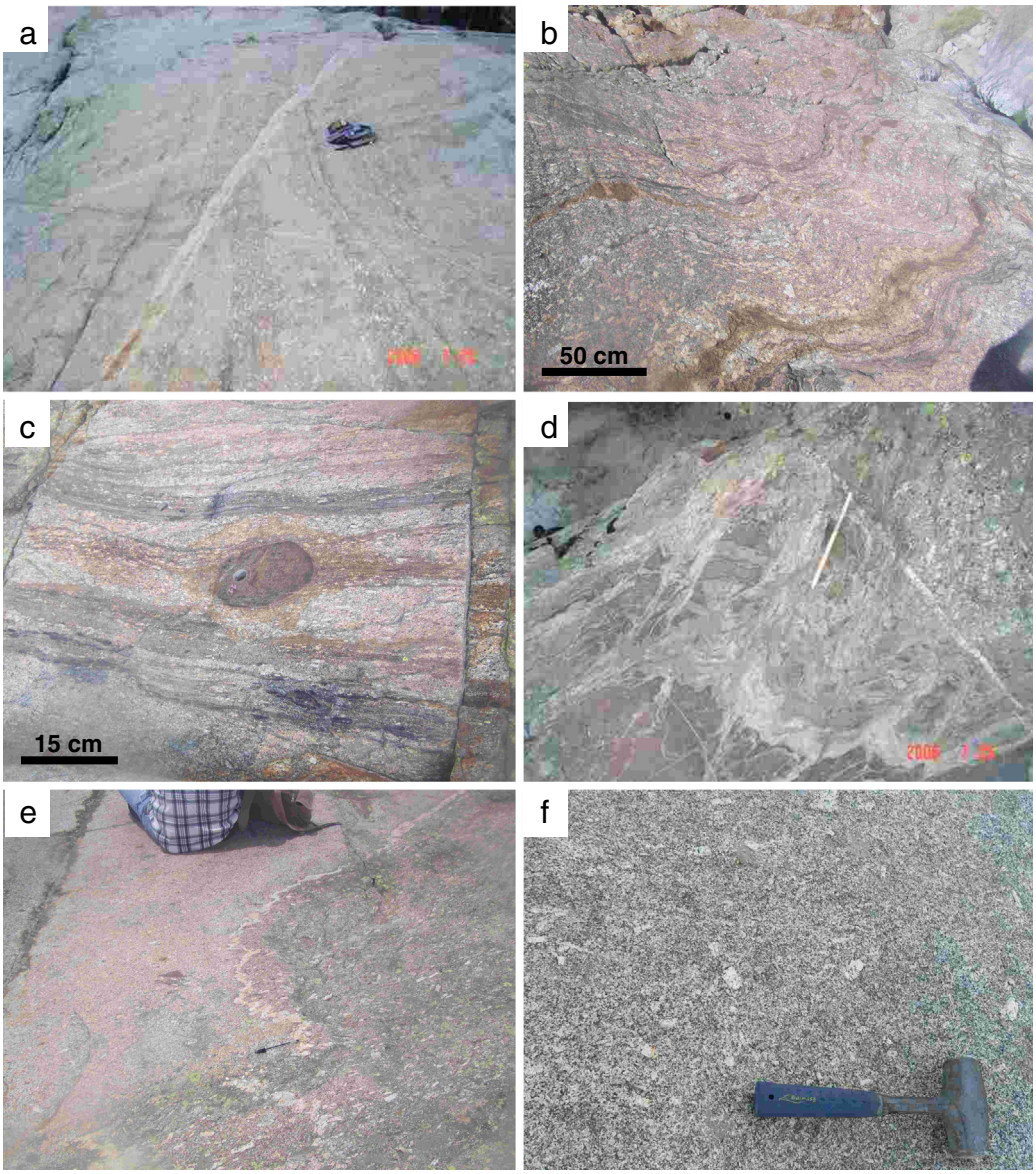

Fig. 3. Field photographs of the main lithologies and structures of the studied area. (a) Circo de Gredos Bt-granodiorite showing the laminar structure of the igneous body. Back-veining of granodiorites by leucogranites generated through partial melting of the host rock metasediments. (b) Magmatic shear zone at the contact between the Circo de Gredos Bt-granodiorite and its overlying metasedimentary body. (c) Magmatic shear zone at the contact between Las Pozas Crd-monzogranite and the Refugio del Rey migmatites. (d) Contact between the Las Pozas Crd-monzogranite and its xenoliths of migmatitic hornfels. Blocks of the metasedimentary body were broken apart and included into the intruding granitoid through progressive brecciation and partial melting. (e) Magmatic contact between the Refugio del Rey leucogranite (left) and the Barbellido-Plataforma intrusive granitoid (right). (f) Barbellido-Plataforma Bt-granodiorite (location of sample J809-1). Note the low volume fraction of Kfs megacrysts and the absence of Crd, which is typical of the inner part of the intruding granitoid sheets, far from their contacts with the metasedimentary host rocks.

analyzed in the SHRIMP II microprobe at Beijing-SHRIMP Center (Chinese Academy of Geological Sciences, Beijing). The mounts were polished to expose the grain interiors, photographed at high magnification in transmitted and reflected light and imaged by SEM (backscattered and CL images) to document the internal growth zoning of the grains. They were then cleaned and coated with high-purity Au in preparation for analysis. Selected areas in zircon grains (spots were chosen to study representative points and features of the studied zircon population), were analyzed for U, Th and Pb isotopes on SHRIMP II ion microprobe at the Research School of Earth Sciences (samples J806-3, J706-47, J806-1, J806-4 and J707-8), and Beijing-SHRIMP Center (sample J809-1), using a procedure similar to that described by Williams and Claesson (1987). A 10 kV negative O_2 primary beam was focused to ca. 20 μm diameter. Positive secondary ions were extracted at 10 kV and mass analyzed at ca. R5000 on a single ETP multiplier by peak stepping through the isotopes of interest. Analytical uncertainties are 1σ precision estimates. All the analyses listed and plotted were corrected for common Pb using the measured ^{204}Pb and a common Pb composition appropriate to the age of each spot (Cummings and Richards, 1975). Concordia ages have been calculated with ISOPLOT 3.0 software (Ludwig, 2003). Uncertainties are 95% confidence limits ($t\sigma$, where t is the student's t multiplier) and include the uncertainty in the Pb/U calibration (ca. 0.3–0.5%). Ages were calculated using the constants recommended by the IUGS Subcommission on Geochronology (Steiger and Jaeger, 1977), with λ errors and MSWD determined using Concord. + Equiv.

4.3. Geochemical analyses

The six samples selected for this zircon geochronological study were previously included in a geochemical study of the Gredos massif

(Díaz Alvarado et al., 2011). About 5 kg of fresh rock was collected at each selected outcrop. Samples were crushed and milled to very fine powder in steel cups. Whole-rock chemistry of major elements and Zr was analyzed by X-ray fluorescence (XRF) at the University of Oviedo (Spain) using glass beads. Precision of the XRF technique was better than ±1.5% relative. Trace elements, including rare earth elements (REE), were analyzed by inductively coupled plasma mass spectrometry (ICP-MS) with an HP-4500 system at the University of Huelva, following digestion in an HF + HNO_3 (8:3) solution, drying and further second dissolution in 3 ml HNO_3. The average precision and accuracy for most of the elements were determined by repeated analyses of the SARM-1 (granite) and SARM-4 (norite) international rock standards, and are in the range 5–10% relative. Data of mineral chemistry were obtained at the University of Huelva with an electron microprobe (JEOL JXA-8200 SuperProbe). A combination of silicates and oxides was used for calibration.

5. Summarized petrology

The petrography and geochemistry of the samples selected for the geochronological study are summarized here (Fig. 4 and Table 2). A more detailed petrologic description of the studied rocks can be seen in Díaz Alvarado et al. (2011) and references therein.

5.1. Bt-granodiorites and monzogranites of Circo de Gredos and Plataforma

Rocks of granodioritic to monzogranitic composition make up the Transitional Intrusive Unit (TIU) of Díaz Alvarado et al. (2011). They are slightly peraluminous granitoids, transitional between the calc-alkalic and alkali-calcic series of Frost et al. (2001), and show good linear trends with tonalites over a wide SiO_2 range from 58 to 71 wt.% in geochemical variation diagrams (Fig. 4). In the CaO–MgO variation diagram these rocks display a good magmatic fractionation trend (Fig. 4c), in clear contrast with the position of Crd-bearing rocks as described below. The studied samples are coarse-grained, mesocratic rocks. They are commonly porphyritic with large Kfs phenocrystals (up to 10 cm length) heterogeneously distributed in bands and irregular patches. They are composed of Qtz, Pl ($An_{32–65}$), Kfs and Bt (Mg# = 31–40). Plagioclases are characterized by a complex oscillatory zoning with repeated resorption surfaces. Common accessory minerals are zircon and apatite.

5.2. Monzogranites of Las Pozas and Barbellido

Rocks of monzogranite composition are mineralogically heterogeneous with variations in the content of Crd and Kfs megacrysts. Monzogranites containing Crd are texturally similar to the Crd-free monzogranites. They share the same grain size, the porphyritic character with large Kfs phenocrysts, and similar Pl compositions ($An_{32–50}$) with complex zoning patterns. However, some local differences in the composition of Bt are found (related to slight differences in Al activity near the contacts with host rocks). Cordierite is usually altered to a fine-grained aggregate of Chl (pinnite) and sericite, always preserving a rectangular prismatic external shape. Monzogranitic rocks containing Crd (from 1 to 12 vol.%) constitute the Alkali-Calcic Unit (ACU) of Díaz Alvarado et al. (2011). The observed mineralogical heterogeneity of these rocks is in agreement with their scattered pattern in geochemical diagrams (Fig. 4). They are medium-high peraluminous granitoids ranging from granodioritic to granitic compositions. In CaO–MgO variation

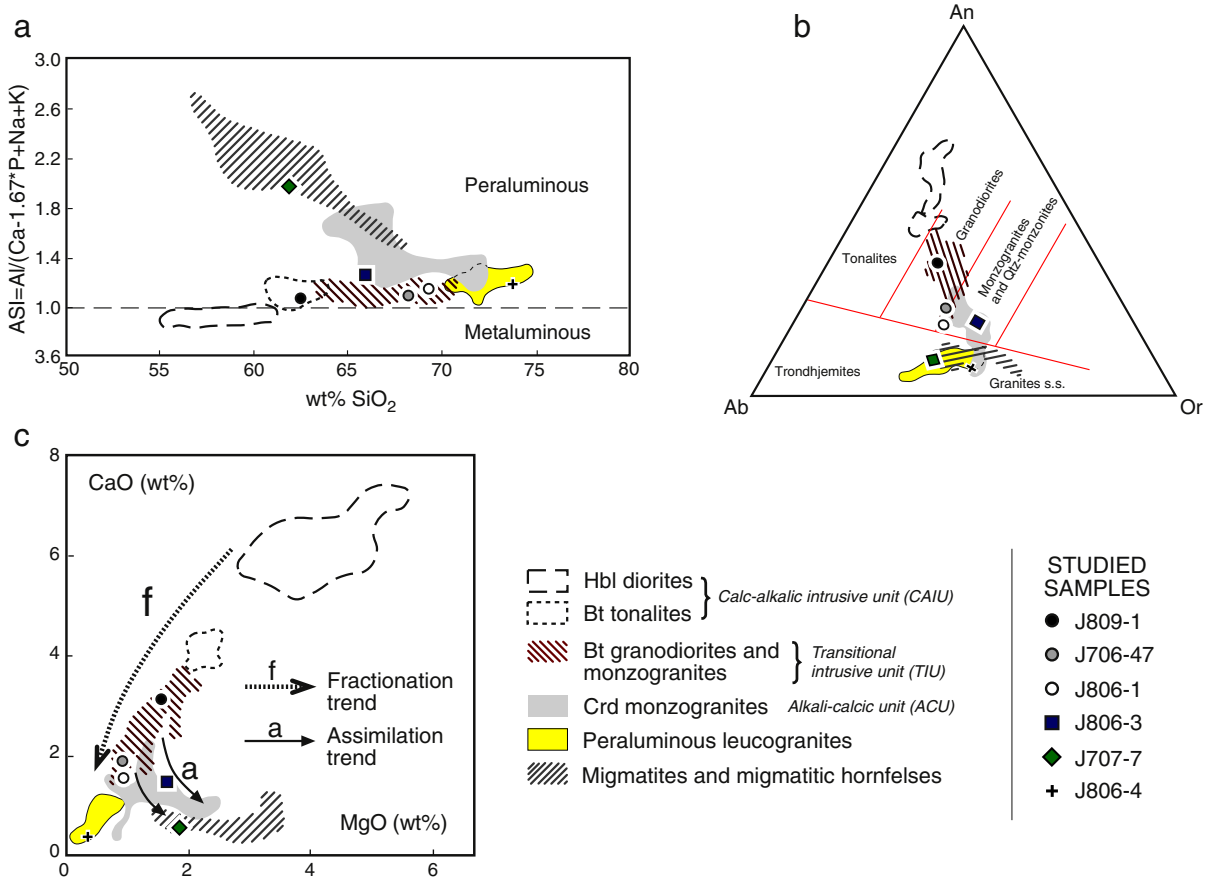

Fig. 4. Plot of the studied granitoids and leucogranites (Table 2) on (a) the granitoid classification diagram of Frost et al. (2001); (b) the classification triangle of O'Connor (1965) for silica-rich rocks (analyzed and not normative feldspars have been plotted in this triangle, due to the departure between normative and real composition of minerals in the studied rocks, a feature that was discussed in detail and interpreted by Díaz Alvarado et al., 2011); and (c) the CaO–MgO variation diagram. The areas depicted in the background represent the main petrologic units defined in the batholith by Díaz Alvarado et al. (2011).

Table 2
Whole-rock composition of the samples selected for the geochronological study of the Gredos massif.

Rock type	Sample	SiO_2[a]	TiO_2	Al_2O_3	FeOt	MgO	MnO	CaO	Na_2O	K2O	P_2O_5	Loi	TOTAL	#Mg[b]	ASI[c]	Zr[d]
Bt granodiorites	J809-1	62.14	0.89	17.14	5.14	1.70	0.10	3.24	3.58	3.94	0.52	0.81	99.20	0.37	1.11	317.6
Bt granodiorites	J706-47	68.19	0.44	16.05	2.69	0.88	0.03	1.91	3.72	4.69	0.14	0.64	99.38	0.37	1.11	125.0
Bt-Crd monzogranites	J806-1	68.97	0.46	15.42	2.80	0.91	0.05	1.47	3.67	4.4	0.19	0.91	99.25	0.37	1.16	126.8
Crd monzogranites	J806-3	65.80	0.76	15.25	4.62	1.48	0.05	1.43	2.80	5.09	0.20	1.45	98.93	0.36	1.22	195.5
Leucogranites	J806-4	74.11	0.22	13.46	1.71	0.37	0.02	0.39	2.93	4.86	0.22	1.09	99.38	0.28	1.28	82.0
Hornfelses	J707-7	61.86	0.65	19.21	4.71	1.83	0.06	0.58	3.13	3.44	0.24	3.26	98.97	0.41	1.99	184.2

[a] wt.%.
[b] #Mg = MgO / (MgO + FeO).
[c] ASI = Al/(Ca − 1.67 ∗ P + Na + K).
[d] ppm.

diagram (Fig. 4c), Crd-monzogranites show a clear departure from cotectic-like trends marked by Bt-granodiorites, which has been interpreted as due to assimilation of pelitic metasediments at the emplacement level (Díaz Alvarado et al., 2011, where it can be found abundant information about the details of this assimilation process).

5.3. Leucogranites of Refugio del Rey

The studied leucogranites from Refugio del Rey are coarse to medium, equigranular, gray-colored, homogeneous rocks, with abundant restites [Bt (Mg# = 39–41) + Sil + Crd (Mg# = 52)] and Qtz-resisters in areas close to the migmatites. Mineral assemblage consists of Qtz, Bt, Ms, Kfs and Pl. Quartz forms anhedral grains with undulose extinction. Biotite (Mg# = 45–49) appears as subhedral to anhedral grains with inclusions of Zrn and, less frequently, Ap, while Kfs shows subhedral grains with perthitic textures. Plagioclase appears as subhedral to anhedral grains, which show normal zonation with cores of oligoclase ($\approx An_{29}$) rimmed by albite ($\approx An_4$). Muscovite forms anhedral to subhedral, mainly primary grains. High-silica leucogranites depart from a linear array with intrusive units in variation diagrams. They are peraluminous granites and are strongly depleted in CaO and MgO (Fig. 4).

5.4. Leucosome of migmatitic hornfelses included in Las Pozas granitoid body

Migmatitic hornfelses appear as xenoliths, to the scale of a few centimeters to tens of meters, hosted by Crd-granodiorites. The paleosome is formed by fine- to medium grained metasediments consisting of metagraywackes interbedded with metaquartzites. The leucosome vein sampled for this study is a fine- to medium-grained, leucocratic vein with allotriomorphic texture. Its mineralogy consists of anhedral Qtz, anhedral to subhedral Kfs, subhedral Pl with cores of oligoclase to andesine ($\approx An_{19-37}$) rimmed by albite to oligoclase ($\approx An_{2-18}$), subhedral Bt (Mg# = 40), anhedral Ms and subhedral to anhedral Crd (Mg# = 52–55) that is more ferric than the average Crd of the paleosome (Mg# = 53–60). Cordierite frequently has inclusions of small, rounded Qtz grains, associated with Zrn grains, and small flakes of Bt. Corroded And grains can occasionally be observed. Accessory assemblage consists mainly of Ap and Zrn. Migmatitic hornfelses and migmatites sampled in the Gredos massif are strongly peraluminous, heterogeneous rocks (Fig. 4). They are plotted together with regional Neoproterozoic sediments (Ugidos et al., 1997, 2008) in geochemical diagrams. Compositions of migmatitic leucosomes and leucogranites are very similar. However, the presence of Crd and restitic minerals originates a scattered distribution of leucogranites and metasediments in geochemical diagrams.

6. U–Pb SHRIMP geochronology

The U–Pb zircon ages obtained in the studied samples are comprised within a time range of around 15 Ma, excluding inherited ages (Supplemental data table). All the analyses included in this geochronological study are statistically and analytically valid. They show discordances lower than 20%, a common Pb content <2%, and the spots are located in areas far from zircon fractures, discontinuities or high luminosity zones (Fig. 5). Exceptions to these analytical characteristics are explained in the detailed description of results. Furthermore, careful study of the morphological features of the analyzed zircons suggests that none of the single age data should be arbitrarily excluded to calculate an average age (concordia age or mean age). Also the geological meaning of such a mean or average age of the entire population seems to be less relevant than a detailed study of the distinct zircon ages obtained at each sample. Therefore, the methodology followed in this work consisted in establishing for each sample several groups with close zircon ages consistent with similar morphological characteristics. The characteristics of the selected zircon populations and the main features and ages of the groups identified in each sample are then described. The studied zircons and their $^{206}Pb/^{238}U$ ages are shown in Fig. 5. Fig. 6 shows the concordia diagrams, the zircon groups and concordia ages. Supplemental data table contains all the analytical results used in this work. Samples J806-3 and J707-7 were reported previously by Díaz Alvarado et al. (2011).

6.1. Circo de Gredos Bt-granodiorite

Analyzed zircons from this sample are shown in Fig. 5. Many of them are large (>250 μm), acicular crystals, with parallel banded or concentric zoning. Some of these zircons exhibit rims that do not show continuity with the internal structure of the crystal, particularly in the apical culmination of the prism. Other abundant crystals are less elongate and show a prominent core, predominantly rounded, with well-developed, concentric overgrowths. Some of these crystals show high luminosity areas (Fig. 5) crossing the zoning pattern that are interpreted as due to dissolution processes. CL images (Fig. 5) show that inherited cores are scarce. Three analyses located in these cores of complex crystals resulted in Proterozoic ages.

Regarding to the late Paleozoic ages, four main groups have been distinguished according to the U–Pb age and morphology of zircons (concordia ages of each group are shown in Fig. 6a). Two analyses yield the oldest $^{206}Pb/^{238}U$ late Paleozoic ages in this sample: 317 ± 3.2 and 322 ± 3.5. These are located in igneous zircons with partially or totally disrupted internal structure, and external concentric rims belonging to a new crystallization phase, at least 5 Ma younger. These analyses, found in cores of compound zircons, fit

Fig. 5. Cathodoluminescence images of the analyzed zircons from the six samples selected for the SHRIMP U–Th–Pb study. Spots' location and $^{206}Pb/^{238}U$ ages are indicated. Data are given in Supplemental data table. Scale bars are 100 μm.

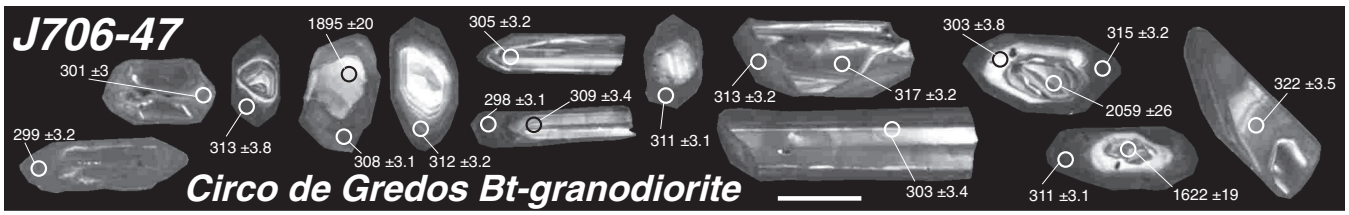
J706-47
301 ±3
313 ±3.8
1895 ±20
308 ±3.1
312 ±3.2
305 ±3.2
298 ±3.1
309 ±3.4
311 ±3.1
313 ±3.2
317 ±3.2
303 ±3.4
303 ±3.8
315 ±3.2
2059 ±26
322 ±3.5
311 ±3.1
1622 ±19
299 ±3.2
Circo de Gredos Bt-granodiorite

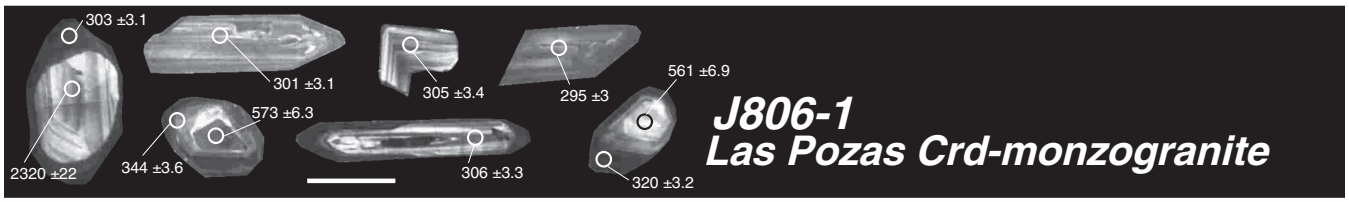
303 ±3.1
301 ±3.1
305 ±3.4
295 ±3
561 ±6.9
573 ±6.3
2320 ±22
344 ±3.6
306 ±3.3
320 ±3.2
J806-1
Las Pozas Crd-monzogranite

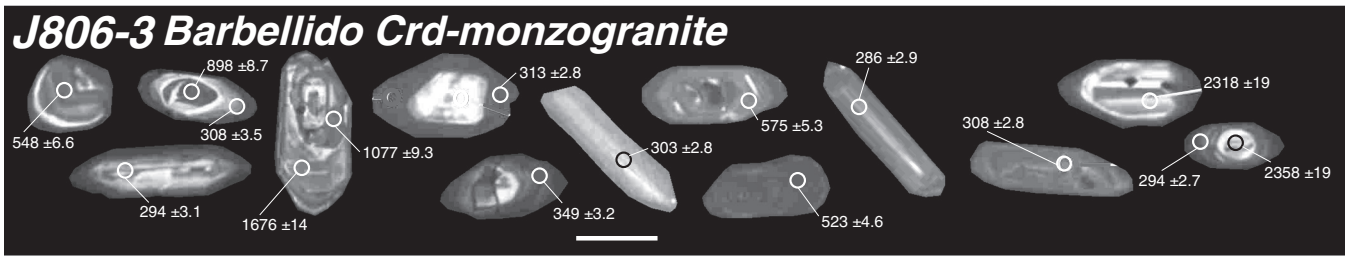
J806-3 Barbellido Crd-monzogranite
898 ±8.7
548 ±6.6
308 ±3.5
1077 ±9.3
313 ±2.8
303 ±2.8
575 ±5.3
286 ±2.9
2318 ±19
308 ±2.8
294 ±2.7
2358 ±19
294 ±3.1
1676 ±14
349 ±3.2
523 ±4.6

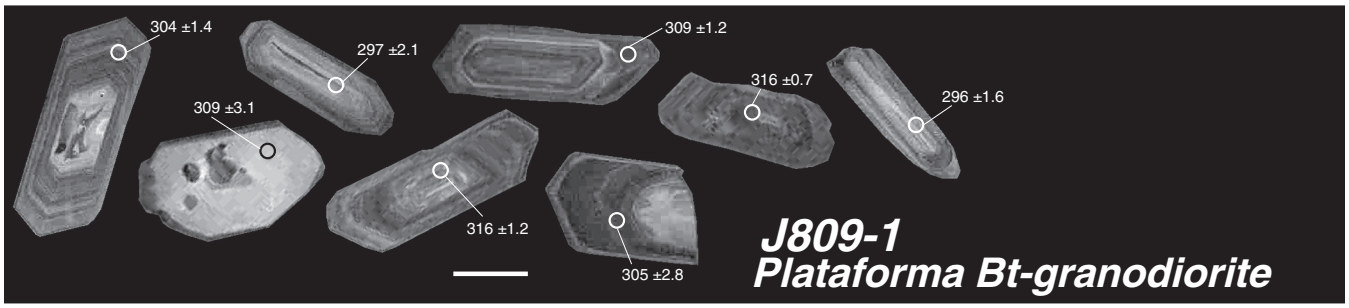
304 ±1.4
297 ±2.1
309 ±1.2
316 ±0.7
296 ±1.6
309 ±3.1
316 ±1.2
305 ±2.8
J809-1
Plataforma Bt-granodiorite

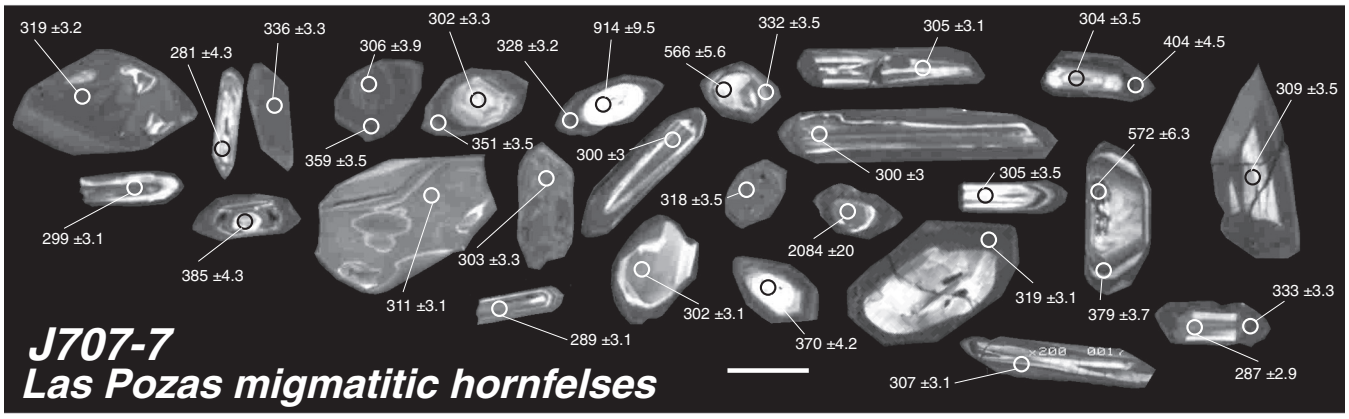
319 ±3.2
281 ±4.3
336 ±3.3
306 ±3.9
302 ±3.3
328 ±3.2
914 ±9.5
566 ±5.6
332 ±3.5
305 ±3.1
304 ±3.5
404 ±4.5
309 ±3.5
359 ±3.5
351 ±3.5
300 ±3
572 ±6.3
305 ±3.5
318 ±3.5
299 ±3.1
385 ±4.3
303 ±3.3
2084 ±20
319 ±3.1
379 ±3.7
333 ±3.3
311 ±3.1
289 ±3.1
302 ±3.1
370 ±4.2
307 ±3.1
287 ±2.9
J707-7
Las Pozas migmatitic hornfelses

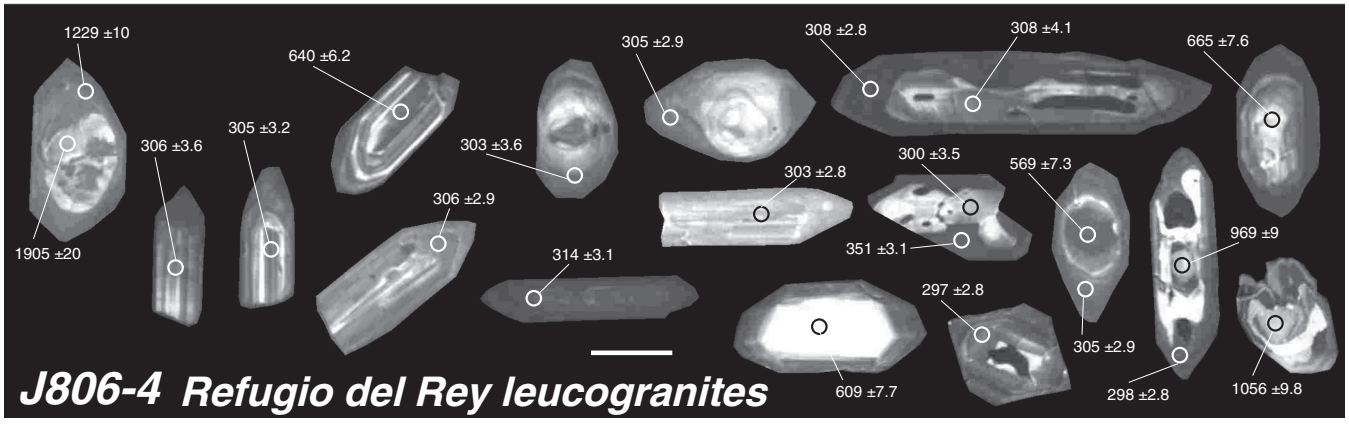
1229 ±10
640 ±6.2
305 ±2.9
308 ±2.8
308 ±4.1
665 ±7.6
306 ±3.6
305 ±3.2
303 ±3.6
303 ±2.8
300 ±3.5
569 ±7.3
1905 ±20
306 ±2.9
351 ±3.1
969 ±9
314 ±3.1
297 ±2.8
305 ±2.9
609 ±7.7
298 ±2.8
1056 ±9.8
J806-4 Refugio del Rey leucogranites

the definition of antecrysts (Hildreth, 2004). The most represented $^{206}Pb/^{238}U$ ages of the sample are between 308 and 315 Ma (Supplemental data table). This group yields a concordia age of 312.6 ± 2.8 Ma (N = 8) (Fig. 6a). Most of these analyses correspond to oscillatory crystal growths over discontinuous cores. Th/U ratios are larger than 0.05. This group is interpreted to define the main crystallization stage of this magmatic body, which is revealed by the nucleation of zircon overgrowths in pre-existing crystals (old inherited zircons and antecrysts). Besides, most small simple acicular zircons give ages younger than those yielded by compound crystals, highlighting the protracted evolution of the crystallization process in the studied magma bodies. An interpretation of this long-lasting evolution will be given in the next sections. Three analyses give a concordia age of 304.1 ± 3.4 Ma (Fig. 6a). Finally, the last group contains the analyses with the youngest ages. These analyses show low Th/U ratios (Supplemental data table) and are located in the most external rims of crystals. These analyses yield a concordia age of 299.7 ± 2.8 Ma (N = 3) (Fig. 6).

6.2. Las Pozas Crd-monzogranite

This sample contains abundant large acicular igneous crystals with parallel banding (Fig. 5). However, smaller, compound zircons are also frequent. Many of the analyses in this sample have been discarded due to various analytical inconsistencies found during the microprobe calibration and the processing of data (excess common Pb, which made the data reduction very difficult). This fact, added to the presence of many inherited ages, caused the short number of late Paleozoic igneous ages determined in this sample. Complex zircons containing inherited cores are here more abundant than in Bt-granodiorite samples. One Paleo to Meso-Proterozoic and two Vendian ages have been found, which are surrounded by oscillatory concentric overgrowths with very low Th/U ratios and late Paleozoic ages: 344.6 ± 3.6 and 320.2 ± 3.2 Ma (Supplemental data table). Most of the analyses with late Paleozoic ages correspond to spots located either in simple acicular crystals or in external overgrowths indistinctly. Four analyses in this group yield a concordia age of 303.5 ± 2.8 Ma (Fig. 6b). In addition, a simple acicular zircon with irregular internal zoning gave a $^{206}Pb/^{238}U$ age of 295 ± 3 Ma.

6.3. Barbellido-Plataforma Crd-monzogranite and Bt-granodiorite

Samples J809-1 (Bt-granodiorite) and J806-3 (Crd-monzogranite) have been studied together because field data indicate that they belong to the same intrusive sheet and, indeed, ages of both samples have resulted very similar (Supplemental data table, Fig. 6c). U–Pb ages in both samples are similar, in the range from 316 to 296 Ma. However, CL images show important morphological differences between zircons of both samples (Fig. 5). Similar to that found in Las Pozas Crd-monzogranite, zircons in the Crd-monzogranite sample (J806-3) are generally small (≈100 μm), short, complex crystals with inherited cores. In contrast, zircons from the Bt-granodiorite sample (J809-1) are large (≈200 μm long), simple, with continuous concentric growths or parallel-banded zoning patterns, which coincides with that observed in the Circo de Gredos Bt-granodiorite. Only a few zircons have high luminosity cores pointing to some type of discontinuity between core and overgrowths (recrystallized or re-equilibrated areas).

Inherited cores have been found only in zircons from sample J806-3 (Crd-monzogranite). U–Pb data show four Paleo- and Meso-Proterozoic ages, three Neo-Proterozoic ages (two of them are Vendian) and one analysis yields a possibly Vendian–Cambrian age. Also one external overgrowth with low Th/U ratio gave a late Paleozoic age (349 ± 3.2 Ma) related to the metamorphic peak (Montero et al., 2004b). In sample J809-1, we have analyzed two prominent cores with parallel-banded zoning interrupted by external oscillatory concentric overgrowths. These characteristics are very similar to those found in the antecryst cores of the Circo de Gredos Bt-granodiorites. Sample J806-3 contains one zircon with similar age, with a high luminosity core that has been ignored due to Pb loss, and an overgrowth with low Th/U ratio (0.02) and a $^{206}Pb/^{238}U$ age of 313 ± 2.8. These three analyses are considered the oldest igneous ages and yield a concordia age of 315.5 ± 1.6 Ma (Fig. 6c). The larger group of ages comprises data between 309 and 303 Ma. These data are obtained analyzing the external oscillatory overgrowths of zircons from both samples, although in the Crd-monzogranite overgrowths occur over inherited cores. One acicular simple crystal is included. These analyses yield a concordia age of 306.9 ± 1.5 Ma (N = 7) (Fig. 6c). Most of small, acicular and parallel-banded zircons gave younger ages. A small overgrowth with Th/U = 0.005 is included in this younger group. Four analyses yield a concordia age of 295.6 ± 1.1 Ma (Fig. 6c). These data are around 10 Ma younger than those determined in the zircons of the previously described group. The youngest age has been obtained in a small acicular zircon ($^{206}Pb/^{238}U$ age = 286 ± 2.9 Ma).

6.4. Leucosome of Las Pozas migmatitic hornfels

The selected zircons from the migmatitic hornfelses are commonly complex, heterogeneous crystals, differing in size and morphology, and some have large U contents (>1%). Most of them are small crystals (80–150 μm) that show a strong morphological variety due to mixing of zircons crystallized from anatectic melts and zircons removed from paleosomes. This sample includes simple acicular zircons, anhedral compound crystals with inherited cores, and crystals with very low luminosity and chaotic zoning (Fig. 5). Some of them show high luminosity cores and low U content. Other cases yield inverted ages (older age for outer rims than for cores). Some apparently inherited cores are indeed low-U areas corresponding to an earlier phase of growth with no discernible age difference between these and their high-U rims.

The number of inherited cores in this sample was less than expected probably due to recrystallization processes. Cores with high luminosity areas in CL images yield ages younger than those of external rims. However, U–Pb ages of inherited zircons are similar to those described in monzogranite samples, two Proterozoic and two Vendian–Cambrian ages. Two Devonian ages, older than the Carboniferous metamorphic peak and younger than the Ordovician ages of some regional metasediments (Bea et al., 2007; Montero et al., 2007; Valverde-Vaquero and Dunning, 2000), have been found. Similar ages have been previously described and assigned to analytical errors or mixed analyses (e.g. Castiñeiras et al., 2008). However, they are similar to the age of nearby Devonian volcanics (Gutiérrez-Alonso et al., 2008). A third analysis with Devonian ages (spot 19.1) has a high discordance that casts doubt on the reliability of the result. However, spots 5.1 (a small, inherited core) and 24.2 (located in the rim of a compound crystal), are analytically correct data (Supplemental data table).

There is an important population of zircons with high U contents, always above 2000 ppm. They are anhedral and show chaotic internal zoning and very low Th/U ratios, which are commonly assigned to metamorphic zircons (Wang et al., 2011; Williams, 1998). The SHRIMP U–Pb calibration in zircons breaks down when the U contents get high. Previous studies have shown that this usually occurs at about 2300–2500 ppm U (McLaren et al., 1994). Zircons of this high U group have been analyzed separately and have not been included in the calculation of average ages. However, $^{207}Pb/^{206}Pb$ ages are not affected by this breakdown of U–Pb calibration, and these age data are presented here for crystals with high U contents. We have distinguished three morphological types within this group: 1) Anhedral crystals with very low luminosity and distinct sizes, showing convolute or chaotic internal zoning pattern. Only spot 18.1 has a Th/U ratio greater than 0.02. Their $^{207}Pb/^{206}Pb$ ages range from 319 to 255 Ma. 2) Overgrowths in

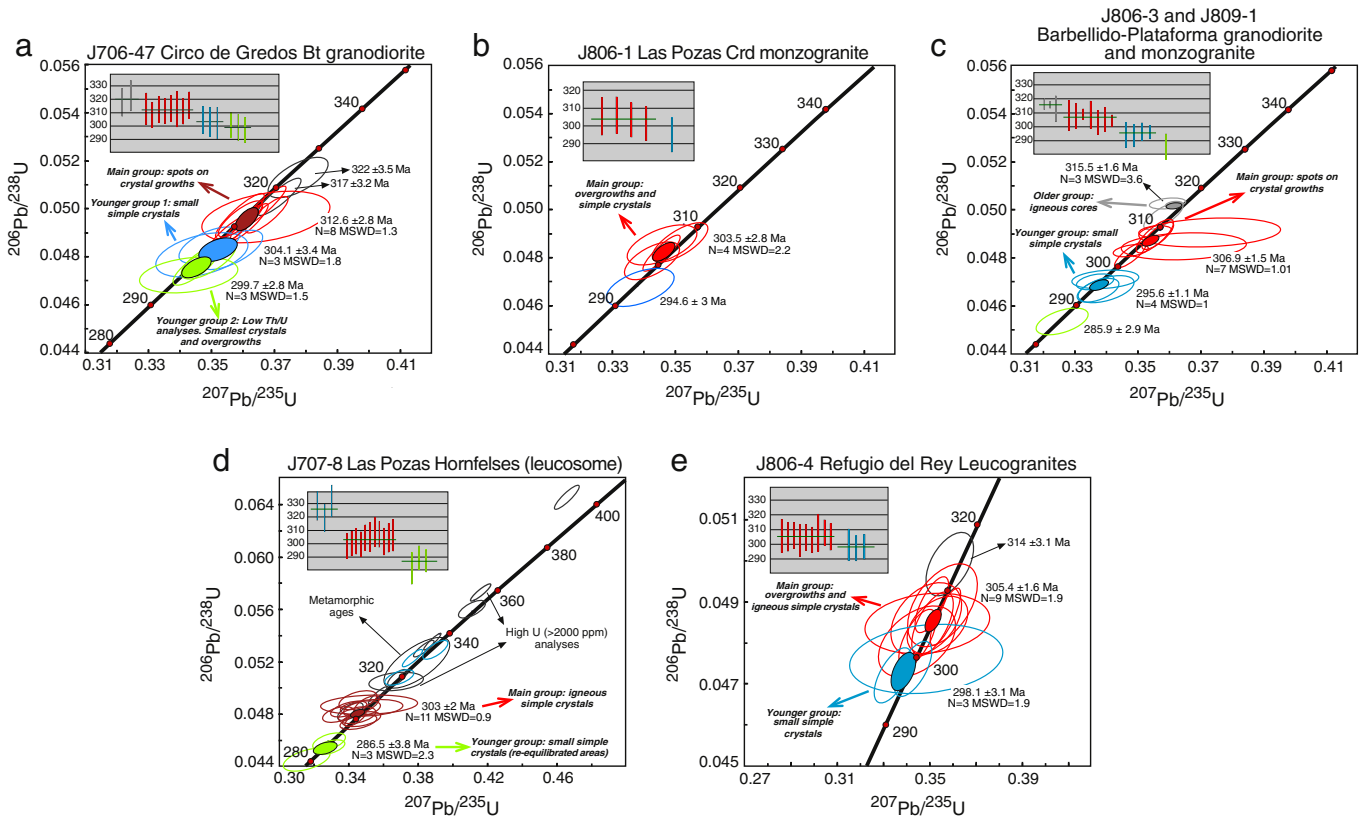

Fig. 6. U–Pb Concordia diagrams of the studied samples. Error ellipses show distinct colors for each group of zircons exhibiting specific morphological features, and mean $^{206}Pb/^{238}U$ ages are indicated. Error ellipses in Concordia diagrams represent a 68.3% conf., including the standard error. Insets show error-bar diagrams (2σ). (a) Concordia diagram of the Circo de Gredos Bt-granodiorite, sample J706-47. (b) Concordia diagram of the Las Pozas Crd-monzogranite, sample J806-1. (c) Concordia diagram of the Barbellido-Plataforma monzogranite and granodiorite, samples J806-3 and J809-1, respectively. (d) Concordia diagrams of zircons from the leucosome of the Las Pozas migmatic hornfelses, sample J707-7. (e) Concordia diagram of the Refugio del Rey leucogranite, sample J806-4. (For interpretation of the references to color in this figure legend, the reader is referred to the web version of this article.)

zircon crystals with inverted ages. All analyses are above 4000 ppm of U (spot 22.2 has 10,000 ppm) and their $^{207}Pb/^{206}Pb$ ages are between 343 and 300 Ma. 3) Overgrowths on inherited cores. They have very low Th/U ratio and their $^{207}Pb/^{206}Pb$ ages are between 349 and 320 Ma. Therefore, the determined ages in this group are very varied, from Early Carboniferous to Permian. Most of these ages coincide with that of regional metamorphism in the Spanish Central System (Table 1). These zircons were present in the anatectic leucogranites as relict crystals during the melting stage of the metasedimentary host rocks.

Therefore, for the purposes of this study we have only considered the ages found in the simple, acicular, parallel-banded crystals, i.e. typical igneous zircons with $^{206}Pb/^{238}U$ ages between 309 and 299 Ma (Supplemental data table). Three analyses on cores with high luminosity (low U) have been included too. These zircons are related to the generation and crystallization of anatectic melts in Las Pozas migmatitic hornfelses yielding a concordia age of 303.0 ± 2 Ma (N = 11) (Fig. 6d). A group of zircons younger than 290 Ma gives a concordia age of 286.5 ± 3.8 Ma (N = 3) (Fig. 6d). These analyses are located in small simple crystals with some evidences of re-equilibrium (disrupted zoning pattern) in external areas, where Pb loss could have occurred.

6.5. Refugio del Rey leucogranites

Selected zircons from the leucogranite sample are large crystals grouped into two main typologies: simple, acicular, parallel-banded zircons, and compound crystals with inherited cores and younger overgrowths. The zircons of this sample are larger in size than those of the leucosomes previously described.

Proterozoic ages are the most represented inherited ages in this sample. Two Cryogenian and two Vendian ages have been determined. One zircon with a high U content and low luminosity yields a $^{206}Pb/^{238}U$ age of 351 ± 3.1 Ma.

One large, simple, acicular crystal, similar to those described below to estimate the main crystallization stage, supplied the oldest age of igneous zircons (314 ± 3.1 Ma). A concordia age of 305.4 ± 1.6 Ma (N = 9) was obtained for the main group of igneous zircons (Fig. 6e), which comprises six analyses located in simple, acicular zircons and three more in external overgrowths of compound crystals (all of them with Th/U > 0.1). The youngest ages are found in zircons with features indicating disequilibrium or dissolution processes. However, excepting spot 13.1, located in a high luminosity area with a high common lead percentage, the rest of analyses are located out of re-equilibrium areas and give a concordia age of 298.1 ± 3.1 Ma (N = 3).

7. Thermal modeling

The results of the geochronological work are pointing to sequential emplacement of granite bodies that, according to previous structural studies, have tabular geometries (Díaz Alvarado et al., 2012). These granitic sheets exhibit a long and complex history of zircon crystallization. In order to put some constraints on the thermal effects on previously emplaced magma bodies of newly emplaced batches, a simple thermal modeling approach has been followed using the finite-element software COMSOL Multiphysics® for the analysis of heat transfer. The heat conduction equation can be written as:

$$\rho C_p \frac{\partial T}{\partial t} + \nabla.(-k\nabla T) = Q,$$

where ρ is the density, C_p is the specific heat capacity at constant pressure, T is the absolute temperature, t is time, k is the thermal conductivity, and Q is heat generation rate per unit volume. This general equation has been applied in 2-D to simulate the thermal evolution of the crust subjected to incremental intrusion of granitic sheets. The aim of this procedure is to find first-order constraints to the problem of maintaining magma chambers for long time periods, as required by the results of zircon geochronology obtained in this work (distinct pulses of zircon growth in the same granitic body, separated by up to several Ma). Distinct types of boundary and initial conditions have been considered. According to the large-scale structure of the studied area (Díaz Alvarado et al., 2012), large sub-horizontal sheets of granite magma of undefined, albeit large, lateral extent and 1 km thickness (Fig. 1, cross section) have been simulated. Accordingly, the model is composed of a set of superposed rectangles 1 km thick and of undefined lateral extension, simulating both the host rocks and the intruding magma batches. Arbitrary widths of 10 km are preferred, because larger values do not modify the final results and considerable enlarge computing times. Boundaries between adjacent rectangles are thermally open to allow vertical heat transfer. Instead, lateral walls are thermally insulated. The upper crust is simulated with 18 rectangles, while similar additional rectangles are added to model the sequential intrusion of granitoid batches. The considered thermal parameters of crustal rocks and magmas are shown in Table 3. Initial temperature inside each rectangle derives from the assumed linear or stepped gradient (see below). An iterative procedure is then applied with the heat transfer module of COMSOL computing the time-dependent temperature distribution of the system for distinct time intervals (Table 3). Temperature profile for subsequent steps at each run is estimated from the dataset of the immediately previous magma intrusion. We have explored twelve runs that model the same sequence of seven intrusions (Fig. 7). The surface (0 km) and basal (18 km before the first magmatic intrusion) temperatures were fixed at 0 °C and 750 °C, respectively. Differences between the modeled runs (Table 3) are the intrusion temperature of the granite sheets (800 °C and 1000 °C) and the time intervals between successive intrusions (100, 300 and 1000 ka), as well as the initial geothermal gradient. The choice of 1000 °C as end-member temperature for magma emplacement seems unreasonably high and it merits some explanation, because it is widely assumed that granites intruded at temperatures as low as 850 °C. Three independent arguments can be proposed to support high temperatures of magma emplacement. First, measured temperatures in granitoids by means of mineral–mineral or mineral–liquid equilibria correspond to near-solidus temperatures. For granodiorite magma intruding at around 850 °C the crystal content will be higher than the rheological threshold and the intrusion process would be inhibited because magmatic flow is prevented at high values of crystallinity (e.g., Petford, 2003; Petford et al., 2000). Second, water-rich magmas may be close to their liquidus at temperatures of the order of 900 °C, saturation will be reached at near liquidus conditions, and granites would be texturally pegmatites with Hbl as the liquidus phase forming large euhedral crystals (see Castro, in press, for a summary of this process). However, the crystallization sequence deduced in the studied region excludes the presence of Hbl as a liquidus phase and it is strongly pointing to reaction from pyroxene to Hbl (Castro and Stephens, 1992). Indeed, the presence of Hbl clots in some granodiorites, derived from pyroxene, is an argument in favor of high T, because the existence of pyroxene in water-bearing magmas implies $T \geq 1000$ °C (Castro, in press). And third, xenoliths of Crd-bearing migmatitic hornfels have been found in the studied area, as described before. Migmatitic hornfelses, rich in Crd, also locally appear as thermal aureoles around the external contacts of the batholith, in the country rocks, where the metamorphic temperatures far from the host-granitoid boundaries barely attained 500 °C (e.g., Rubio Pascual et al., 2013, post-D2 metamorphic conditions of their upper unit). For a pressure of 4 kbar at the studied batholith (Pereira, 1993; Pereira and Bea, 1994), the wet solidus for pelitic schists is of about 650 °C (e.g., Le Breton and Thompson, 1988), while the temperature for peritectic reactions of water-undersaturated partial melting generating cordierite in the studied migmatitic hornfelses must have attained at least 750 °C (Castro et al., 2000; Díaz Alvarado et al., 2011). Taking into account the initial temperature of the low-grade country rocks (around 500 °C), and following the equation of heat conduction across a plane contact (Carslaw and Jaeger, 1959), the temperature of the intruding magma should have exceeded that of generation of the migmatitic hornfelses from 150 °C (water-saturated melting) to 250 °C (water-undersaturated melting). Therefore, temperatures of 800 °C and 1000 °C for the magma at the intrusion level are considered as realistic end-member conditions for thermal simulation.

Two initial geothermal gradients have been applied. First, a linear gradient of 41.66 °C/km (125 °C every 3 km), which is a reasonable estimation for the syn-D2 to syn-D3 high-T and low- to intermediate-P metamorphism of Central Iberia (e.g., Castiñeiras et al., 2008; Pereira and Bea, 1994; Rubio Pascual et al., 2013). As described before, the intrusion of the main bodies exploited active extensional detachments (e.g., Díaz Alvarado et al., 2012), which, together with the structure resulting from the previous extensional D2 phase, explains the local presence of low-grade country rocks and xenoliths (transformed into migmatitic hornfelses by repeated intrusion of granitoid magmas) in an area dominated by granitic bodies and anatectic complexes. The second geothermal gradient consists of a linear gradient from the surface (0 °C) up to 13 km depth (750 °C), while downwards the temperature remains constant at 750 °C (the estimated temperature of migmatites in the studied area, Pereira, 1993; Pereira and Bea, 1994). This sort of stepped gradient implies the presence of a large domain of high, steady temperatures at depth. This high-T domain can be due to the thermal effect of repeated magmatic intrusions (see below and Fig. 8), or to lithospheric thinning caused by orocline development (e.g., Gutiérrez-Alonso et al., 2011a, b). The effect of latent heat of crystallization and enthalpy of melting has not been included in the thermal modeling and therefore the model can be considered only as a first approach to the studied problem. Besides, latent heat of magma crystallization and enthalpy of melting of host-rock are believed to partially cancel (e.g., Bowers et al., 1990), such that their influence on the first-order results presented here must not to be large. Taking into account this limitation, the estimated final temperatures should be considered as minimum values. The other relevant parameters used in the models are indicated in Table 3.

The final geotherm varies depending on the considered model. For granitic magmas intruded at 800 °C the predicted geotherms attain the granite solidus at depths larger than at least 13 km or 12 km for a initial linear or stepped gradient, respectively (Fig. 8a,c). Decreasing the time interval between successive intrusions yields higher final geothermal gradients. Host rocks (country rock plus

Table 3
Parameters for thermal models.

Run	L1, S1	L2, S2	L3, S3	L4, S4	L5, S5	L6, S6
Intruding magma temperature (°C)	800	800	800	1000	1000	1000
Interval between magma pulses (ka)	100	300	1000	100	300	1000
Parameters		Host rock			Granitic magma	
Density (kg/m^3)		2600[a]			2510[a]	
Thermal conductivity (W/m K)		2.0[b]			1.5[c]	
Heat capacity (J/kg K)		1390[d]			1450[a]	

L and S refer to linear and stepped initial geothermal gradient, respectively (see text for more explanation).
[a] Asimow and Ghiorso (1998) and Ghiorso and Sack (1995).
[b] Whittington et al. (2009).
[c] Clauser and Huenges (1995).
[d] Gutiérrez and Parada (2010).

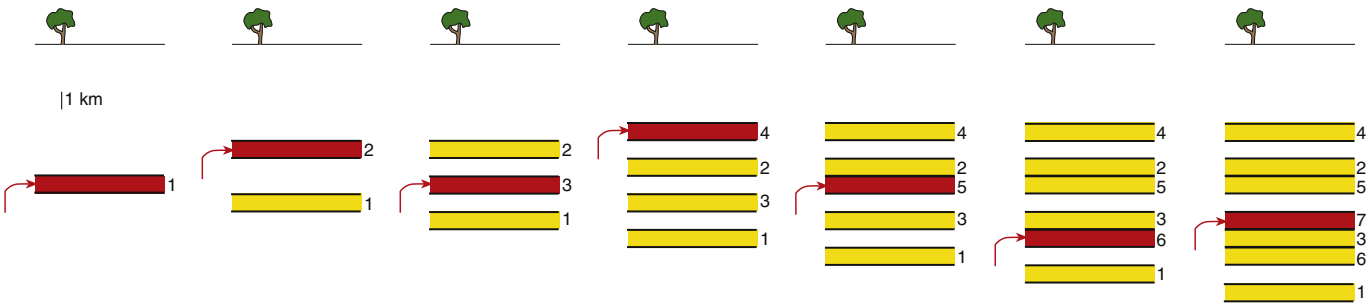

Fig. 7. Sketch depicting the chosen sequence of emplacement of seven tabular magmatic bodies (from 1 to 7) at the middle crust. The sequence is the same for the twelve runs studied in this work (Table 3).

earlier cooled intrusions) rise toward zircon saturation temperature only for the more restrictive conditions (initial stepped geotherm, interval of 100 ka between intrusions; Fig. 8c). In contrast, magmas intruded at 1000 °C predict geothermal gradients (Fig. 8b,d) that reach and even exceed the zircon saturation temperature for a wide range of controlling boundary conditions (intervals of 100 and 300 ka and initial linear or stepped geotherms). An interesting outcome is that, starting from an initial linear geotherm, a hot, partially melted domain, several km thick, appears at depth (Fig. 8a,b). This feature is less marked for magmas intruded at 800 °C (Fig. 8a) and for long time intervals (1000 ka) between successive magma batches. Indeed, the runs simulating a stepped linear geotherm

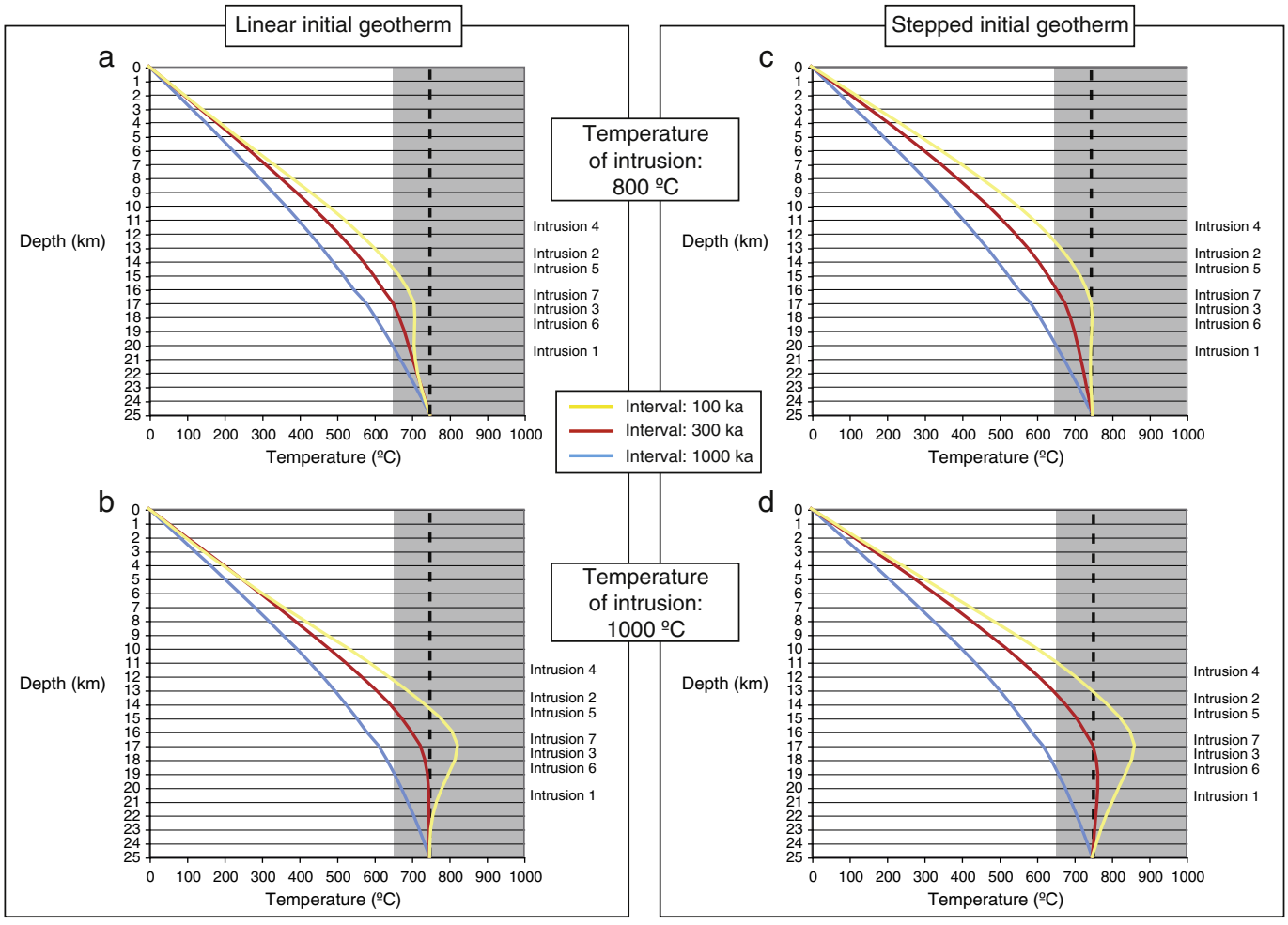

Fig. 8. Final modeled geothermal gradients. The model considers seven successive magma sheets (see Fig. 7), 1 km thick each, that intrude the upper-middle crust. The yellow, red and blue lines display the calculated geotherm assuming regular time intervals of 100, 300 and 1000 ka, respectively, between the seven successive intrusions. Each geotherm was computed 100 (yellow lines), 300 (red lines) or 1000 (blue lines) ka after the end of the final (#7) emplacement. Left column: linear initial geotherm. Right column: stepped initial geotherm. Upper row (a and c): results considering that the successive magma sheets intruded at 800 °C. Lower row (b and d): results considering that the successive magma sheets intruded at 1000 °C. The gray area outlines the approximate super-solidus region for granitic compositions (≥650 °C, Johannes, 1984; Johannes and Holtz, 1996; Tuttle and Bowen, 1958). The vertical, bold dashed line approximately corresponds to zircon saturation in peraluminous anatectic melts (Miller et al., 2003; Watson and Harrison, 1983) and also to the estimated migmatitic conditions in the studied area (Pereira, 1993; Pereira and Bea, 1994). (For interpretation of the references to color in this figure legend, the reader is referred to the web version of this article.)

(Fig. 8c,d) can be envisaged as indirectly resulting from the intrusion of 7 new granitic bodies into a crust affected by a previous process of thermal maturation (Fig. 8a,b).

8. Discussion

The geochronological study of intrusive granitoids and anatectic melts of the Gredos massif shows that it is possible to find in a single sample a range of ages that greatly exceeds the time required for the emplacement and crystallization of a granitic magma within the middle to upper crust (e.g., Petford et al., 2000). These wide age ranges are not due to analytical errors, as shown in the previous sections. The U–Pb ages recorded in zircons from intrusive granitoids and anatectic leucogranites of the studied area define a long-living process spanning from ca. 320 to 290 Ma. However, the obtained age data are not evenly distributed across the entire range and gaps of more than 5 Ma have been identified. Zircons with similar ages display common morphological characteristics, which is the basis for the identification of age groups described in the previous section (Fig. 6). Determination of the main stages of zircon crystallization is a useful tool to discuss magma evolution, emplacement history and relationships among the distinct granitic bodies.

8.1. Emplacement sequence

The presence of inherited zircons in some samples must be related to local assimilation processes (xenocrysts), in accordance with field observations, experimental and geochemical data (Díaz Alvarado et al., 2011). This issue is evident in the intrusive sheet of Barbellido-Plataforma, where the two selected samples yield very similar ages and only differ due to the presence of inherited cores, which also affects the morphology of the zircons (Fig. 5), in sample J806-3, close to the contact with the metasedimentary complex, and its absence in sample J809-1, far from this contact.

Fig. 9a shows the relative probability histograms of the studied intrusive granitoids and leucogranitic melts. Interestingly, these diagrams (see also Fig. 9b,c) are very similar to the probability plots presented by Gutiérrez-Alonso et al. (2011a) summarizing an exhaustive population of U–Pb age data of granitoids and mafic rocks from the Central Iberian Zone. These data are pointing to an extensive tectono-magmatic process that affected the central and northern part of the Iberian Variscan massif during the Late Carboniferous and Early Permian, which is reinforced by the age data presented in this work. However, it must be stressed that our analysis is focused on the study of intra-sample U–Pb age variability and it is not particularly interested on the large-scale implications of a multi-sample (and multi-pluton) statistics of age data. Examples of the characteristic zircons in each peak of age frequency are attached to the histograms showing the relationship between morphology and the main U–Pb ages analyzed. The profiles of these histograms repeat a similar pattern for the three samples of intrusive granitoids. Prior to the main stage of crystallization, the older ages (between 322 and 317 Ma for Circo sample, and between 316 and 313 Ma for Barbellido-Plataforma sample) correspond to analyses on apparently igneous cores showing no continuity with the outer and younger areas of these zircons. These ages do not appear in sample J806-1 (Las Pozas Crd-monzogranites) probably due to the smaller amount of analyses. These zircons are considered antecrysts (in the sense of Hildreth, 2004) and can be assigned to the first stage of magma crystallization. Afterwards, dissolution of these zircons took place. Processes able to generate large differences (several millions of years) in the ages of a population of magmatic zircons in a given sample are not yet well known. Putative causes are changes in composition and temperature of the magma chamber, or the existence of a multi-chamber system at various crustal levels. The study of pressure determination from the analysis of zircon geochemistry (i.e., Bingen et al., 2004; Gao et al., 2011) could shed some light on these processes. Preliminary constraints to the effects of temperature changes are advanced in this work.

The main peak of age frequency appears at distinct ages for the three intrusive granitoids (Fig. 9a,b), about 312.6, 306.9 and 303.5 Ma for the samples taken from the bottom (Circo de Gredos), upper (Barbellido-Plataforma) and middle (Las Pozas) granitic sheets, respectively. Most of these ages were determined on outer rims in complex zircons. The main stage of igneous zircon crystallization in intrusive granitoids likely took place at the emplacement level. In all the studied samples, zircons of this age are the most abundant and they commonly appear as rims grown over inherited crystals interpreted as xenocrysts according to two lines of evidences. First, these inherited cores are absent in the samples located far from the metasedimentary country rocks. Second, the ages of the cores (Paleo- to Meso-Proterozoic, Vendian and Vendian–Cambrian, Early Carboniferous) are coincident to those found in the analyzed zircons sampled in the metasediments and their associated anatetic granites (Proterozoic, Early Cambrian, late Devonian to Early Carboniferous).

However, ages younger than the main crystallization age can be found over a range of 10 to 15 Ma in all samples (Fig. 9a). In the Circo de Gredos sample, the younger frequency peaks coincide with the main crystallization ages in Barbellido-Plataforma and Las Pozas intrusive sheets. This pattern is similar to those observed in anatectic granites and leucosomes, where the main frequency peaks are coeval or immediately later than the main crystallization stages in their nearby intrusive granitoids (Fig. 9c). These repeated age patterns allow us elucidating the emplacement sequence of the studied granitic bodies. The main stages of zircon crystallization in the intrusive bodies (Fig. 9b,c) are here suggested to correspond to their main emplacement event, as explained before. According to this, the older magma batch emplaced in the study area was the Circo de Gredos Bt-granodiorite sheet, followed by the Barbellido-Plataforma and the Las Pozas Crd-monzogranite bodies (Fig. 9b). The main stage of zircon crystallization in the Refugio del Rey leucogranite occurs immediately after the corresponding main stage of the Barbellido-Plataforma intrusive sheet (Fig. 9c), which overlies the anatectic complex. This supports field observations that show co-magmatic contacts between granodiorites and anatectic leucogranites. The same can be said of the leucosomes of migmatitic hornfelses regarding the Las Pozas sheet, where the metasedimentary xenoliths are contained.

8.2. Significance of the distinct mean age groups. Thermal effects of sequential emplacement

The magmatic evolution of each granitic body should have spread over several million years (Fig. 9), although the presence of a main stage of zircon crystallization is pointing, within a protracted, slow and punctuated cooling process, to the likely interval of maximum growth that could correspond to the time period where the major volume of magma was emplaced. Accepting that the main group of zircon ages constrains the emplacement period of each magmatic sheet, the presence of older and younger age groups deserves an explanation. The antecrysts can be interpreted as the result of early stages of sequential growth of each granite sheet. Alternatively, antecrysts can have been picked up in transit or from local precursors at the emplacement level. In any case, cooling happened fast enough to avoid complete dissolution before temperature fell to saturation level.

Interpretation of younger age groups requires special attention. A possible explanation is that they correspond to intrusion of new granitoid batches in the same chamber (recharge) or in nearby areas (sequential emplacement of distinct sheets), mimicking the migmatization of host rocks due to the thermal effects of granitic magma emplacement (Fig. 9c). Actually, the younger ages in the Circo de Gredos Bt-granodiorite are contemporary to the intrusion of Las Pozas body atop of it (Fig. 9b). Similarly, the younger ages in

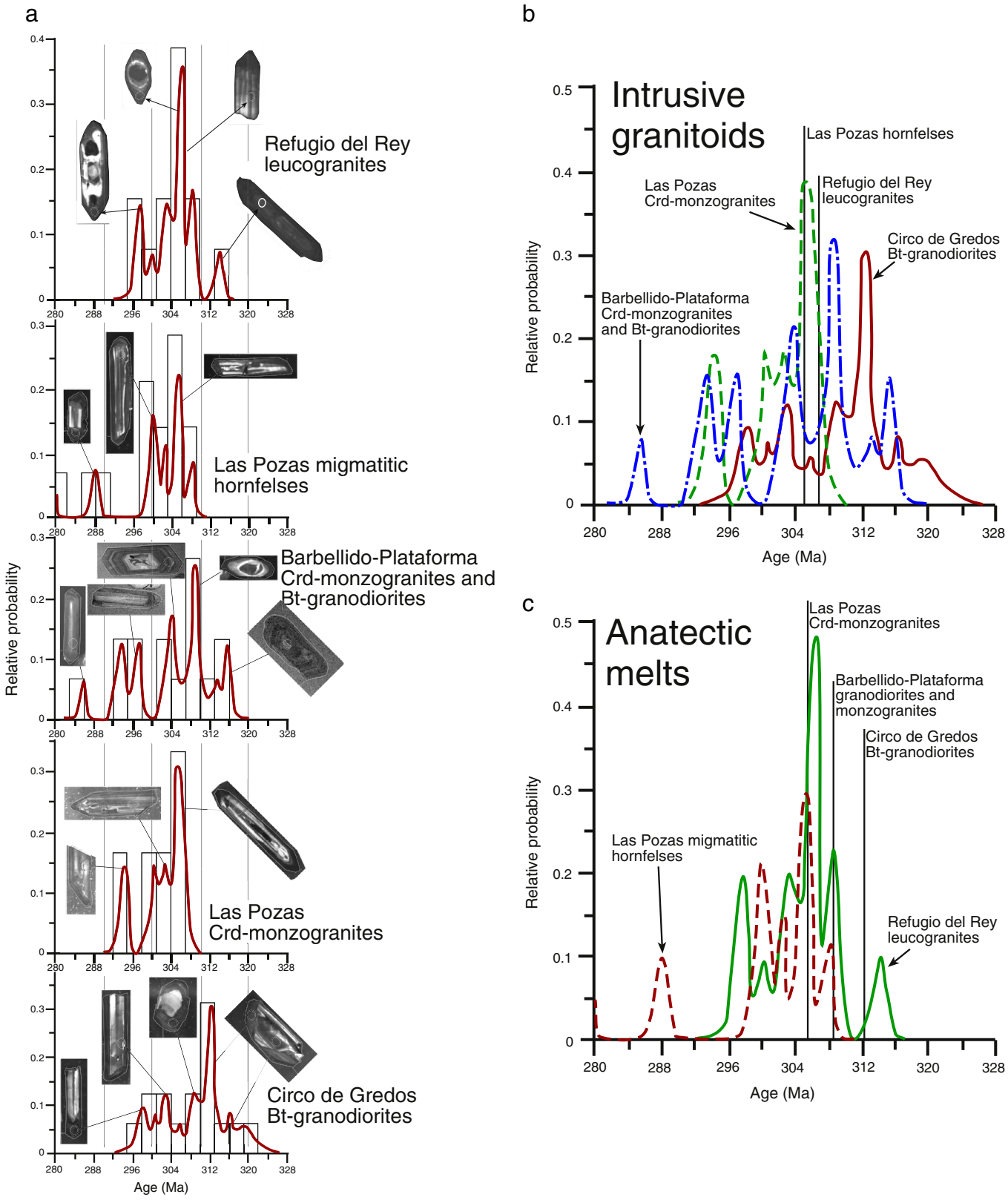

Fig. 9. Relative probability histograms showing the main populations of U–Pb ages analyzed in the studied samples. Histograms are referred to the igneous or intrusive stage, so that the inherited ages are not included. (a) Probability plots. Photographs of selected zircon crystals for the distinct probability maxima are included. (b) Probability density distribution of the three intrusive granodioritic and monzogranitic bodies showing the characteristics of the main age groups analyzed and described in each sample. Maxima of the age density distribution of anatectic melts are added for comparison. (c) Probability density distribution in the two samples of anatectic leucogranites. The main maxima of the age density distribution of the three intrusive granitoids are also depicted to reveal the age relation between granodioritic intrusion and melt generation in the metasedimentary host rocks at the emplacement level.

Barbellido-Plataforma and Las Pozas sheets could be explained with 295 Ma-old magmatic inputs located outside, albeit not far from, the studied area. Therefore, the shape of the intrusive granitic bodies (Fig. 1) and the geochronological results of this work (Fig. 9) strongly support a model of sequential emplacement of distinct sheets to explain the distribution of zircon ages determined at each sample. This interpretation requires that the distinct granitic sheets remained in a magmatic state for very long periods (>5 Ma), able to become rejuvenated by successive intrusions.

A possible constraint to this late assertion can be provided by thermal modeling. Very few studies have examined up to date the thermal evolution of sequentially built batholiths (e.g., Annen et al., 2006; Hanson and Glazner, 1995; Paterson et al., 2007, 2011). A simple model to evaluate the feasibility of keeping long-living super-solidus temperatures on an incrementally growing batholith has been implemented in this work (Figs. 7, 8). One of the more relevant parameters in this process is the temperature of zircon saturation in magma (T_{Zr}), which depends on magma composition. According to Watson and Harrison (1983) and Miller et al. (2003), this relationship can be expressed by the equation:

$$T_{Zr} = 12,900/[2.95 + 0.85\,M + \ln(496,000/Zr_{melt})],$$

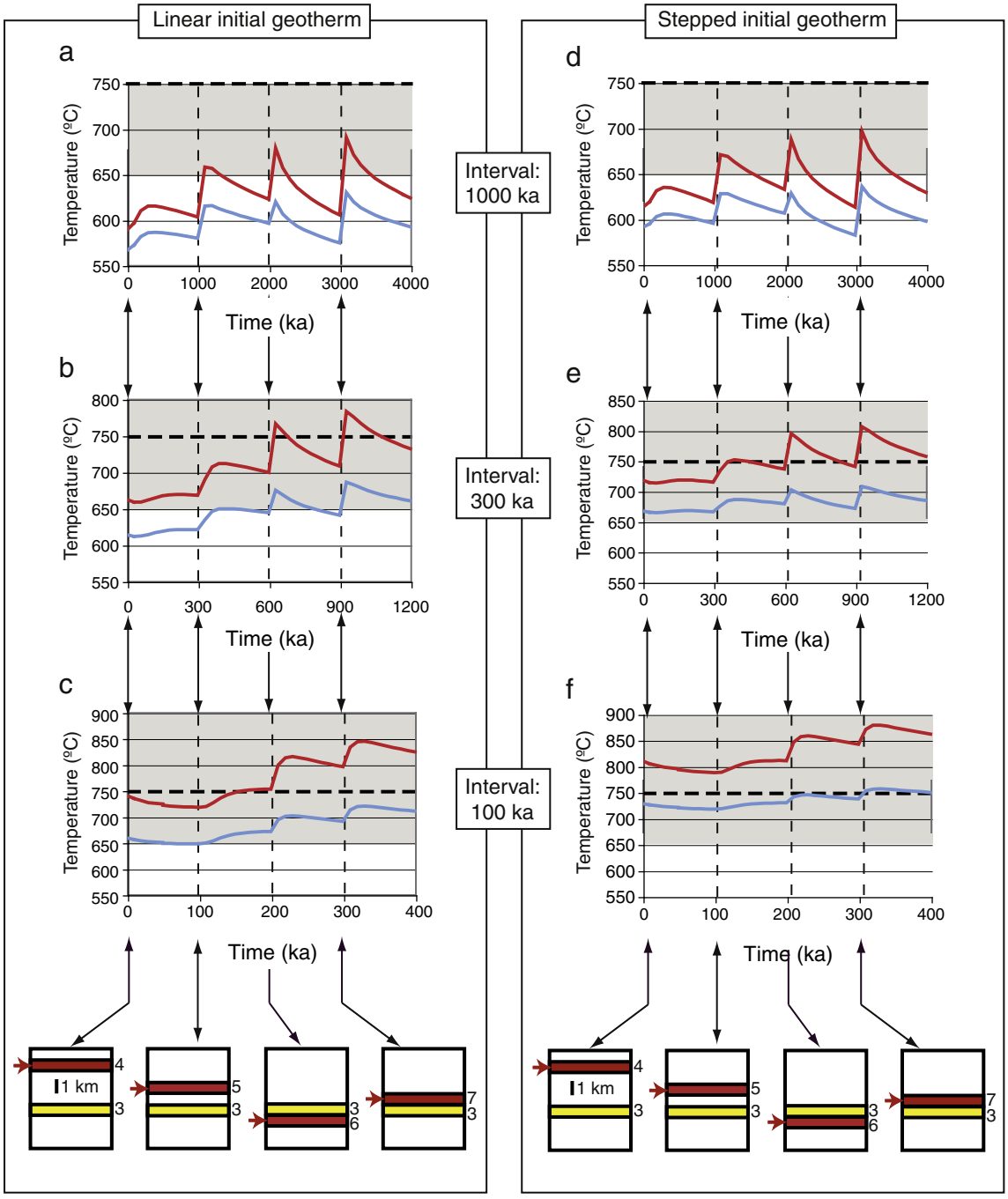

Fig. 10. Time evolution of temperatures at the center of granitic intrusion #3 (see Fig. 7). Red and blue lines show temperature paths computed considering that successive magma batches intruded at initial temperatures of 1000 °C and 800 °C, respectively. (a, b, c) Initial linear geotherm and intervals between intrusions of 1000 ka (a), 300 ka (b) and 100 ka (c). (d, e, f) Initial stepped geotherm and intervals between intrusions of 1000 ka (d), 300 ka (e) and 100 (ka). The gray area marks the super-solidus region for granitic magmas while the horizontal, bold dashed lines approximately corresponds to zircon saturation in peraluminous anatectic melts (see main text). (For interpretation of the references to color in this figure legend, the reader is referred to the web version of this article.)

where M is a compositional factor which depends on silica content and peraluminosity of the melt (Miller et al., 2003). Accordingly, T_{Zr} for the studied samples are between 814 °C calculated for Bt-granodiorites (J809-1) and 763 °C for leucogranites (J806-4). These results coincide with the temperatures measured by Miller et al. (2003) to define "hot" and "cold" granites, respectively. Considering that the granodioritic intrusive magma started crystallizing mainly during its emplacement, which seems a reasonable assumption according to geochemical and structural information (Díaz Alvarado et al., 2011, 2012), residual melt must have reached a composition close to that of peraluminous leucogranites (Castro et al., 2000; Patiño Douce and Johnston, 1991), so that zircon saturation temperatures in the already emplaced granitoids would have been very similar to that of anatectic melts (763 °C for sample J806-4).

The results of the thermal modeling followed in this work show that the process of sequential intrusion of granitic batches could lead to the generation of a high-temperature (≥650 °C), migmatitic domain at the crustal zone that is being intruded by granodioritic layers (Fig. 8). It is relevant here to consider the time evolution of temperatures within a given granitic body. To illustrate this evolution, a point located at the center of intrusion 3 (Fig. 7) has been selected. Following emplacement of granitic sheets 4 to 7, the temperature at the center of intrusion 3 oscillates. A first interesting observation is that the rising of temperature is larger (up to 90 °C) if the intruding sheet is located above the reference point (larger temperature increases after intrusion of body 7 than in other cases in Fig. 10). Second, this temperature increase is directly related to the time interval between successive pulses (compare, for instance, Fig. 10a and c), which coincides with previous estimations (e.g., Annen, 2011). Third, the temperature within the analyzed body remains in super-solidus conditions for long time periods, in some cases even for the entire considered duration of the experimental run (Fig. 10b to e). This feature is more marked for short intrusion time intervals and high initial magma temperatures. Fourth, the zircon saturation temperature in residual melts is exceeded cyclically or permanently for intermediate and short intrusion time intervals (300 and 100 ka, respectively) and high initial magmatic temperatures (1000 °C, Fig. 10b to f). On the other side, the model is unable to attain the zircon saturation temperature in the residual melt of the granitic sheets for intruding temperatures of 800 °C, unless very extreme conditions are considered (stepped geotherm and intervals shorter than 100 ka between magma pulses, Fig. 10f). However, it must be said that this not completely exclude the sequential resorption and growth of zircon crystals under low initial magma temperatures (800 °C), because melt fraction must cyclically increase and, therefore, some zircon must dissolve into it to maintain saturation levels of Zr. These theoretical results predict time separations of only around 300 ka (e.g., Fig. 10b) for consecutive episodes of zircon growth, which contrasts with the geochronological determinations presented in this work (groups of zircon ages separated for several Ma). To account for this apparent discrepancy, it is important to acknowledge that the model presented here is only a first approximation with many simplifications (see section of thermal modeling) and it must be considered as a mere qualitative test of the feasibility of the process of sequential zircon growth in a given magmatic body. Also, the three analyzed bodies (Circo de Gredos, Las Pozas and Barbellido-Plataforma) are only a very reduced sample of the vast number of granite sheets of the Gredos massif. Many other tabular bodies are above, and below those of the studied area (Banda et al., 1981 mentioned the presence of a layer more than 10 km thick of granitic crust in the area at the present time, according to geophysical information), therefore theoretically

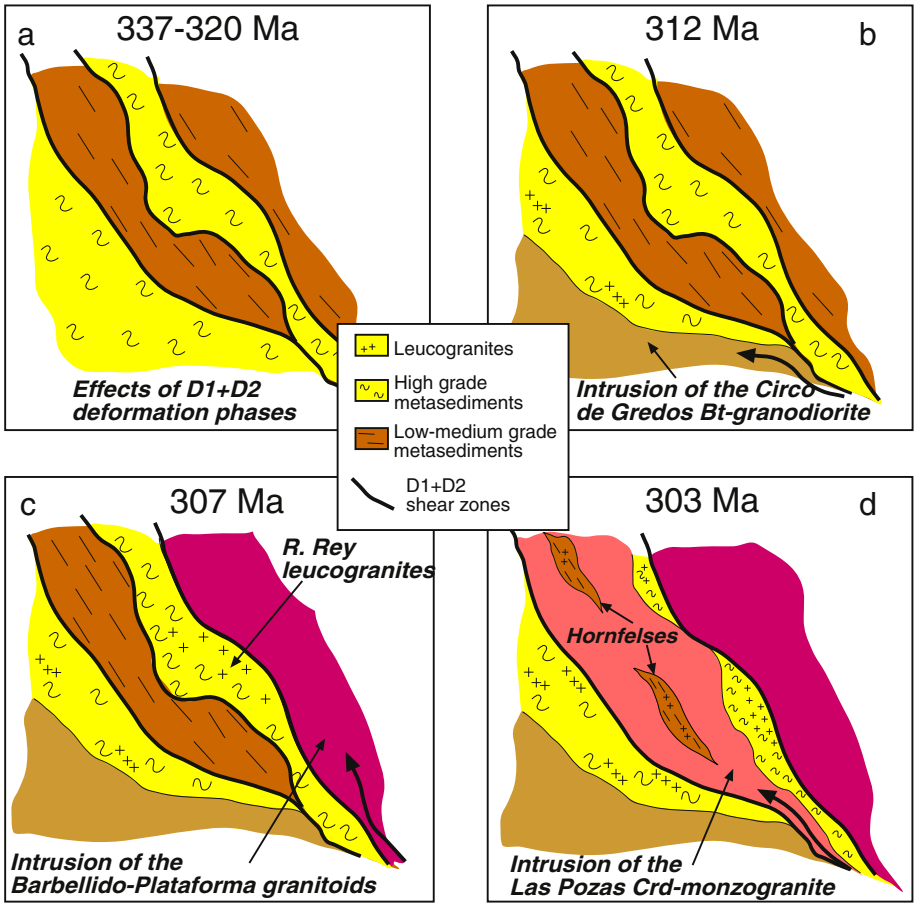

Fig. 11. Idealized 2D sketch depicting the time evolution of the distinct granitoid sheets of the studied area. The pictures approximately represent the present-day plan-view surface.

allowing long lasting periods of survival of magmatic systems with repeated zircon partial dissolution and new growth events (much longer than those shown in Fig. 10).

Therefore, according to the constraints imposed by the thermal modeling, the repeated intrusion process could have thermally rejuvenated the previously emplaced bodies, favoring the permanence over extended periods of time (several million years) of partially melted host rocks and magmatic bodies that retained a significant melt percentage. Temperatures in these magmatic bodies fluctuated with each new intrusion or group of intrusions around values near zircon saturation, resulting in the distinct age groups observed in this work at a given sample. Fig. 11 proposes a sketch of sequential intrusion of granitic magmas in the studied area according to the ages obtained in this geochronological study.

9. Conclusions

The zircon geochronology is an essential tool to understand the magmatic evolution and emplacement mechanism of large batholiths composed of distinct magma pulses. A result of the use of this technique is to establish the intrusion sequence and the relations between magma emplacement and the geochemical and structural evolution of the batholith. Nevertheless, many intricate details of the zircon U–Th–Pb isotopic data are elusive and remain still to be deciphered. Among these is the wide range of zircon ages found in one given sample. In this work, the statistically valid SHRIMP U–Pb analyses of zircon have been grouped according to the obtained age and the morphological characteristics of zircons. The mean age of these groups is here interpreted as indicative of the distinct stages of zircon crystallization in the granitic magma. Some groups with old ages are considered as antecrysts or xenocrysts. The main zircon group, containing most of the analyzed zircons in a given sample, is interpreted as due to the main emplacement episode, which is based on the morphological characteristics of the zircons, among other criteria. It is here hypothesized that the groups with younger crystals can be understood as a consequence of the thermal evolution of the batholith due to sequential emplacement of a large number of magma batches (zircons from three of them have been analyzed here and seven theoretical bodies have been used in the numerical model, but many more granitoid sheets are exposed in the Gredos region). A simple numerical model has been implemented to put some qualitative constraints into this hypothesis. Comparison of the several determined groups among the distinct studied granitoid bodies and their host rocks is a key technique to understand the complex process of emplacement and interaction of the intrusive magma pulses originating the batholith.

According to the data presented in this work, the main period of granitoid magma intrusion took place between 312.6 $\pm$ 2.8 Ma and 303.5 $\pm$ 2.8 Ma in the studied zone of the Gredos massif, contemporary with the extensional episodes of the regional Late Paleozoic D3 deformation phase. The intrusive sequence started with the Circo de Gredos Bt-granodiorite and it was followed with the emplacement of the Barbellido-Plataforma granodiorite and monzogranite and finally, the Las Pozas Crd-monzogranite. A time gap of 4–5 Ma has been here determined between the studied magmatic pulses.

Supplementary data to this article can be found online at http://dx.doi.org/10.1016/j.lithos.2013.05.006.

Acknowledgments

This work is part of the PhD Thesis of J.D.A., carried out at the Departments of Geology and Geodynamics and Palaeontology, University of Huelva, with a Grant Fellowship from the Spanish Ministry of Science and Innovation (grant no. AP2005-3498). The work was funded with Projects CGL2004-06808-CO4-01/BTE, CGL2004-06808-CO4-02/BTE, CGL2007-63237/BTE, and CGL2010-22022-CO2-01 of the Spanish Ministry of Science and Innovation. Richard Armstrong assisted with SHRIMP work at ANU, Canberra. We are grateful for constructive peer reviews by Calvin Miller and Gabriel Gutiérrez-Alonso, and colleague reviews by José María Tubía, Gabriel Gutiérrez-Alonso, Miguel López-Plaza, Guillermo Corretgé and M. Francisco Pereira, all of which improved the manuscript.

References

Annen, C., 2011. Implications of incremental emplacement of magma bodies for magma differentiation, thermal aureole dimensions and plutonism–volcanism relationships. Tectonophysics 500, 3–10.
Annen, C., Scaillet, B., Sparks, R.S.J., 2006. Thermal constraints on the emplacement rate of a large intrusive complex: the Manaslu leucogranite, Nepal Himalaya. Journal of Petrology 47, 71–95.
Asimow, P.D., Ghiorso, M.S., 1998. Algorithmic modifications extending melts to calculate subsolidus phase relations. American Mineralogist 83, 1127–1131.
Bachmann, O., Bergantz, G.W., 2004. On the origin of crystal-poor rhyolites: extracted from batholithic crystal mushes. Journal of Petrology 45, 1565–1582.
Bachmann, O., Dungan, M.A., Lipman, P.W., 2002. The Fish Canyon magma body, San Juan volcanic field, Colorado; rejuvenation and eruption of an upper-crustal batholith. Journal of Petrology 43, 1469–1503.
Banda, E., Suriñach, E., Aparicio, A., Sierra, J., Ruiz de la Parte, E., 1981. Crust and upper mantle structure of the central Iberian Meseta (Spain). Geophysical Journal of the Royal Astronomical Society 67, 779–789.
Bea, F., Montero, P., Molina, J.F., 1999. Mafic precursors, peraluminous granitoids, and late lamprophyres in the Avila batholith: a model for the generation of Variscan batholiths in Iberia. Journal of Geology 107, 399–419.
Bea, F., Montero, P., Zinger, T., 2003. The nature, origin, and thermal influence of the granite source layer of Central Iberia. Journal of Petrology 111, 579–595.
Bea, F., Villaseca, C., Bellido, F., 2004. El Batolito de Ávila (Sistema Central Español). In: Vera, J.A. (Ed.), Geología de España. SGE-IGME, Madrid, pp. 101–110.
Bea, F., Montero, P., González Lodeiro, F., Talavera, C., Molina, J.F., Scarrow, J.H., Whitehouse, M.J., Zinger, T., 2006. Zircon thermometry and U–Pb ion-microprobe dating of the gabbros and associated migmatites of the Variscan Toledo anatectic complex, Central Iberia. Journal of the Geological Society of London 163, 847–855.
Bea, F., Montero, P., González-Lodeiro, F., Talavera, C., 2007. Zircon inheritance reveals exceptionally fast crustal magma generation processes in Central Iberia during the Cambro-Ordovician. Journal of Petrology 48, 2327–2339.
Belousova, E.A., Griffin, W.L., O'Reilly, S.Y., Fisher, N.J., 2002. Igneous zircon: trace element composition as an indicator of source rock type. Contributions to Mineralogy and Petrology 143, 602–622.
Bingen, B., Austrheim, H., Whitehouse, M.J., Davis, W.J., 2004. Trace element signature and U–Pb geochronology of eclogite-facies zircon, Bergen Arcs, Caledonides of W Norway. Contributions to Mineralogy and Petrology 147, 671–683.
Bowers, J.R., Kerrick, D.M., Furlong, K.P., 1990. Conduction model for the thermal evolution of the Cupsuptic aureole, Maine. American Journal of Science 290, 644–665.
Burgisser, A., Bergantz, C.W., 2011. A rapid mechanism to remobilize and homogenize highly crystalline magma bodies. Nature 471, 212–215.
Capdevila, R., Corretge, G., Floor, P., 1973. Les granitoides varisques de la Meseta Ibérique. Bulletin de la Société Géologique de France 15, 209–228.
Carslaw, H.S., Jaeger, J.C., 1959. Conduction of Heat in Solids. Clarendon Press, Oxford.
Casquet, C., Montero, P., Galindo, C., Bea, F., Lozano, R., 2004. Geocronología $^{207}Pb/^{206}Pb$ en cristal único de circón y Rb–Sr del plutón de La Cabrera (Sierra del Guadarrama). Geogaceta 35, 71–74.
Castiñeiras, P., Villaseca, C., Barbero, L., Martín Romera, C., 2008. SHRIMP U–Pb zircon dating of anatexis in high-grade migmatite complexes of central Spain: implications in the Hercynian evolution of Central Iberia. International Journal of Earth Sciences 97, 35–50.
Castro, A., 2013. Tonalite–granodiorite suites as cotectic systems: a review of experimental studies with application to granitoid petrogenesis. Earth-Science Reviews (in press).
Castro, A., Stephens, E.W., 1992. Amphibole-rich polycrystalline clots in calc alkaline granitic rocks and their enclaves. Canadian Mineralogist 30, 1093–1112.
Castro, A., Corretgé, L.G., El-Biad, M., El-Hmidi, H., Fernández, C., Patiño Douce, A., 2000. Experimental constraints on Hercynian Anatexis in the Iberian Massif, Spain. Journal of Petrology 41, 1471–1488.
Castro, A., Corretgé, L.G., De La Rosa, J., Enrique, P., Martínez, F.J., Pascual, E., Lago, M., Arranz, E., Galé, C., Fernández, C., Donaire, T., López, S., 2002. Paleozoic magmatism. In: Gibbons, W., Moreno, M.T. (Eds.), The Geology of Spain. Geological Society, London, pp. 117–153.
Chappell, B.W., Stephens, W.E., 1988. Origin of infracrustal (I-type) granite magmas. Transactions of the Royal Society of Edinburgh, Earth Sciences 79, 71–86.
Chappell, B.W., White, A.J.R., 1974. Two contrasting granite types. Pacific Geology 8, 173–174.
Clauser, C., Huenges, E., 1995. Thermal conductivity of rocks and minerals. In: Ahrens, T.J. (Ed.), Rock Physics–Phase Relations. A Handbook of Physical Constants. American Geophysical Union, Washington DC, pp. 105–126.
Coleman, D.S., Gray, W., Glazner, A.F., 2004. Rethinking the emplacement and evolution of zoned plutons: geochronologic evidence for incremental assembly of the Tuolumne Intrusive Suite, California. Geology 32, 433–436.
Cummings, G.L., Richards, J.R., 1975. Ore lead isotope ratios in a continuously changing Earth. Earth and Planetary Science Letters 28, 155–171.
Dallmeyer, R.D., Martínez Catalán, J.R., Arenas, R., Gil Ibarguchi, J.I., Gutiérrez-Alonso, G., Farias, P., Aller, J., Bastida, F., 1997. Diachronous Variscan tectonothermal

activity in the NW Iberian Massif: evidence from $^{40}Ar/^{39}Ar$ dating of regional fabrics. Tectonophysics 277, 307–337.
Dias, G., Leterrier, J., Mendes, A., Simoes, P.P., Bertrand, J.M., 1998. U–Pb zircón and monazite geochronology of post-collisional Hercynian granitoids from the Central Iberian Zone (Northern Portugal). Lithos 45, 349–369.
Díaz Alvarado, J., Castro, A., Fernández, C., Moreno-Ventas, I., 2011. Assessing bulk assimilation in cordierite-bearing granitoids from the Central System batholith, Spain; experimental, geochemical and geochronological constraints. Journal of Petrology 52, 223–256.
Díaz Alvarado, J., Fernández, C., Díaz Azpiroz, M., Castro, A., Moreno-Ventas, I., 2012. Fabric evidence for granodiorite emplacement with extensional shear zones in the Variscan Gredos massif (Spanish Central System). Journal of Structural Geology 42, 74–90.
Escuder Viruete, J., Arenas, R., Martínez Catalán, J.R., 1994. Tectonothermal evolution associated with Variscan crustal extension in the Tormes Gneiss Dome (NW Salamanca, Iberian Massif, Spain). Tectonophysics 238, 1–22.
Escuder Viruete, J., Hernáiz Huerta, P.P., Valverde-Vaquero, P., Rodríguez Fernández, R., Dunning, G., 1998. Variscan syncollisional extension in the Iberian Massif: structural, metamorphic and geochronological evidence from the Somosierra sector of the Sierra de Guadarrama (Central Iberian Zone, Spain). Tectonophysics 290, 87–109.
Farina, F., Dini, A., Innocenti, F., Rocchi, S., Westerman, D.S., 2010. Rapid incremental assembly of the Monte Capanne pluton (Elba Island, Tuscany) by downward stacking of magma sheets. Geological Society of America Bulletin 122, 1463–1479.
Fernández, C., Castro, A., 1999. Pluton accommodation at high strain rates in the upper continental crust. The example of the Central Extremadura batholith, Spain. Journal of Structural Geology 12, 1143–1149.
Fernández, C., Becchio, R., Castro, A., Viramonte, J.M., Moreno-Ventas, I., Corretgé, L.G., 2008. Massive generation of atypical ferrosilicic magmas along the Gondwana active margin: implications for cold plumes and back-arc magma generation. Gondwana Research 14, 451–473.
Frost, B.R., Barnes, C.G., Collins, W.J., Arculus, R.J., Ellis, D.J., Frost, C.D., 2001. A geochemical classification for granitic rocks. Journal of Petrology 42, 2033–2048.
Galindo, C., Huertas, M.J., Casquet, C., 1994. Cronología Rb–Sr y K–Ar de diques de la Sierra de Guadarrama (Sistema Central Español). Geogaceta 16, 23–26.
Gao, X.-Y., Zheng, Y.-F., Chen, Y.-X., 2011. U–Pb ages and trace elements in metamorphic zircon and titanite from UHP eclogite in the Dabie orogen: constraints on P–T–t path. Journal of Metamorphic Geology 29, 721–740.
Ghiorso, M.S., Sack, R.O., 1995. Chemical mass transfer in magmatic processes IV. A revised and internally consistent thermodynamic model for the interpolation and extrapolation of liquid–solid equilibria in magmatic systems at elevated temperatures and pressures. Contributions to Mineralogy and Petrology 119, 197–212.
Glazner, A.F., Bartley, J.M., Coleman, D.S., Gray, W., Taylor, R.Z., 2004. Are plutons assembled over millions of years by amalgamation from small magma chambers. GSA Today 14, 4–11.
Gutiérrez, F., Parada, M.A., 2010. Numerical modeling of time-dependent fluid dynamics and differentiation of a shallow basaltic magma chamber. Journal of Petrology 51, 731–762.
Gutiérrez-Alonso, G., Murphy, J.B., Fernández-Suárez, J., Hamilton, M.A., 2008. Rifting along the northern Gondwana margin and the evolution of the Rheic-Ocean: a Devonian age for the El Castillo volcanic rocks (Salamanca, Central Iberian Zone). Tectonophysics 461, 157–165.
Gutiérrez-Alonso, G., Fernández Suárez, J., Jeffries, T.E., Johnston, S.T., Pasto-Galán, D., Murphy, J.B., Franco, M.P., Gonzalo, J.C., 2011a. Diachronous post-orogenic magmatism within a developing orocline in Iberia, European Variscides. Tectonics 30. http://dx.doi.org/10.1029/2010TC002845.
Gutiérrez-Alonso, G., Murphy, J.B., Fernández-Suárez, J., Weil, A.B., Franco, M.P., Gonzalo, J.C., 2011b. Lithospheric delamination in the core of Pangea: Sm–Nd insights from the Iberian mantle. Geology 39, 155–158.
Hanson, R.B., Glazner, A.F., 1995. Thermal requirements for extensional emplacement of granitoids. Geology 23, 213–216.
Hildreth, W., 2004. Volcanological perspectives on Long Valley, Mammoth Mountain and Mono Craters: several contiguous but discreet systems. Journal of Volcanology and Geothermal Research 136, 169–198.
Huber, C., Bachmann, O., Manga, M., 2010. Two competing effects of volatiles on heat transfer in crystal-rich magmas: thermal insulation vs defrosting. Journal of Petrology 51, 847–867.
Huber, C., Bachmann, O., Dufek, J., 2011. Thermo-mechanical reactivation of locked crystal mushes: melting-induced internal fracturing and assimilation processes in magmas. Earth and Planetary Science Letters. http://dx.doi.org/10.1016/j.epsl.2011.02.022.
Jeon, H., Williams, I.S., Chappell, B.W., 2012. Magma to mud to magma: rapid crustal recycling by Permian granite magmatism near the eastern Gondwana margin. Earth and Planetary Science Letters 319–320, 104–117.
Johannes, W., 1984. Beginning of melting in the granite system Qz–Or–Ab–An–H_2O. Contributions to Mineralogy and Petrology 86, 264–273.
Johannes, W., Holtz, F., 1996. Petrogenesis and Experimental Petrology of Granitic Rocks. Springer, Berlin.
Kretz, R., 1983. Symbols for rock-forming minerals. American Mineralogist 68, 277–279.
Le Breton, N., Thompson, A.B., 1988. Fluid-absent (dehydration) melting of biotite in metapelites in the early stages of crustal anatexis. Contributions to Mineralogy and Petrology 99, 226–237.
Ludwig, K.R., 2003. Isoplot 3.0—a geochronological toolkit for Microsoft Excel. Special Publication No. 4.Berkeley Geochronology Center, Berkeley, California (71 pp.).
Martínez Catalán, J.R., Fernández Suárez, J., Jenner, G.A., Belousova, E., Díez Montes, A., 2004. Provenance constraints from detrital zircon U–Pb ages in the northwestern Iberian Massif: implications for Paleozoic plate configuration and Variscan evolution. Journal of the Geological Society of London 161, 461–473.
McLaren, A.C., Fitz Gerald, J.D., Williams, I.S., 1994. The microstructure of zircon and its influence on the age determination from Pb/U isotopic ratios measured by ion microprobe. Geochimica et Cosmochimica Acta 58, 993–1005.
Miller, C.F., McDowell, S.M., Mapes, R.W., 2003. Hot and cold granites? Implications of zircon saturation temperatures and preservation of inheritance. Geology 31, 529–532.
Miller, C.F., Furbish, D.J., Walker, B.A., Claiborne, L.L., Koteas, G.C., Bleick, H.A., Miller, J.S., 2011. Growth of plutons by incremental emplacement of sheets in crystal-rich host: evidence from Miocene intrusions of the Colorado River region, Nevada, USA. Tectonophysics 500, 65–77.
Montero, P., Bea, F., Zinger, T., 2004a. Edad $^{207}Pb/^{206}Pb$ en cristal único de circón de las rocas máficas y ultramáficas del sector de Gredos, Batolito de Ávila (Sistema Central Español). Revista de la Sociedad Geológica de España 17, 157–167.
Montero, P., Bea, F., Zinger, T.F., Scarrow, J.H., Molina, J.F., Whitehouse, M., 2004b. 55 million years of continuous antexis in Central Iberia: single-zircon dating of the Peña Negra Complex. Journal of the Geological Society of London 161, 255–263.
Montero, P., Bea, F., González-Lodeiro, F., Talavera, C., Whitehouse, M.J., 2007. Zircon ages of the metavolcanic rocks and metagranites of the Ollo de Sapo Domain in central Spain: implications for the Neoproterozoic to Early Palaeozoic evolution of Iberia. Geological Magazine 144, 963–976.
Moreno-Ventas, I., Rogers, G., Castro, A., 1995. The role of hybridization in the genesis of Hercynian granitoids in the Gredos massif, Spain: inferences from Sr–Nd isotopes. Contributions to Mineralogy and Petrology 120, 137–149.
O'Connor, J.T., 1965. A classification for quartz-rich igneous rocks based on feldspar ratios. United States Geological Survey Professional Paper B525, 79–84.
Paterson, S.R., Okaya, D., Matzel, J., Memeti, V., Mundil, R., 2007. Size and longevity of magma chambers in the Tuolumne batholith: a comparison of thermal modeling and cooling thermochronology. Eos, Transactions of the American Geophysical Union 88, 52.
Paterson, S.R., Zák, J., Janouzek, V., 2008. Growth of complex sheeted zones during recycling of older magmatic units into younger: Sawmill Canyon area, Tuolumne batholith, Sierra Nevada, California. Journal of Volcanology and Geothermal Research 177, 457–484.
Paterson, S.R., Okaya, D., Memeti, V., Economos, R., Miller, R.B., 2011. Magma addition and flux calculations of incrementally constructed magma chambers in continental margin arcs: combined field, geochronologic, and thermal modeling studies. Geosphere 7, 1439–1468.
Patiño Douce, A.E., Johnston, A.D., 1991. Phase equilibria and melt productivity in the pelitic system: implications for the origin of peraluminous granitoids and aluminous granulites. Contributions to Mineralogy and Petrology 107, 202–218.
Pereira, M.D., 1993. Termobarometría de rocas con la asociación granate–cordierita - biotita; trayectorias P–T en el complejo anatéctico de la Peña Negra (Batolito de Ávila). Implicaciones sobre el metamorfismo hercínico en la Zona Centro Ibérica. Revista de la Sociedad Geológica de España 6, 131–140.
Pereira, M.D., Bea, F., 1994. Cordierite-producing reactions in the Peña Negra complex, Avila batholith, Central Spain: the key role of cordierite in low-pressure anatexis. Canadian Mineralogist 32, 763–780.
Petford, N., 2003. Rheology of granitic magmas during ascent and emplacement. Annual Review of Earth and Planetary Sciences 31, 399–427.
Petford, N., Cruden, A.R., McCaffrey, K.J.W., Vigneresse, J.L., 2000. Granite magma formation, transport and emplacement in the Earth's crust. Nature 408, 669–673.
Ramsay, J.G., 1967. Folding and Fracturing of Rocks. McGraw-Hill, New York.
Rodríguez Alonso, M.D., Díez Balda, M.A., Perejón, A., Pieren, A., Liñán, E., López Díaz, F., Moreno, F., Gámez Vintaned, J.A., González Lodeiro, F., Martínez Poyatos, D., Vegas, R., 2004. Dominio del Complejo Esquisto-grauváquico. Estratigrafía. La secuencia litoestratigráfica del Neoproterozoico-Cámbrico inferior. In: Vera, J.A. (Ed.), Geología de España. IGME-SGE, Madrid, pp. 78–81.
Rubio Pascual, F.J., Arenas, R., Martínez Catalán, J.R., Rodríguez Fernández, L.R., Wijbrans, J.R., 2013. Thickening and exhumation of the Variscan roots in the Iberian Central System: tectonothermal processes and $^{40}Ar/^{39}Ar$ ages. Tectonophysics 587, 207–221.
Steiger, R., Jaeger, E., 1977. Subcommission on geochronology: convention on the use of decay constants in geo- and cosmochronology. Earth and Planetary Science Letters 36, 359–362.
Tuttle, O.F., Bowen, N.L., 1958. Origin of granites in the light of experimental studies in the system $NaAlSi_3O_8$–$KAlSi_3O_8$–SiO_2–H_2O. Geological Society of America, Memoirs 74.
Ugidos, J.M., Valladares, M.I., Recio, C., Rogers, C., Fallick, A.E., Stephens, W.E., 1997. Provenance of Upper Precambrian–Lower Cambrian shales in the Central Iberian Zone, Spain: evidence from a chemical and isotopic study. Chemical Geology 136, 55–70.
Ugidos, J.M., Stephens, W.E., Carnicero, A., Ellam, R.M., 2008. A reactive assimilation model for regional-scale cordierite-bearing granitoids: geochemical evidence from the Late Variscan granites of the Central Iberian Zone, Spain. Earth and Environmental Science Transactions of the Royal Society of Edinburgh 99, 225–250.
Valle Aguado, B., Azevedo, M.R., Schaltegger, U., Martínez Catalán, J.R., Nolan, J., 2005. U–Pb zircon and monazite geochronology of Variscan magmatism related to syn-convergence extension in Central Northern Portugal. Lithos 82, 169–184.
Valverde-Vaquero, P., Dunning, G.R., 2000. New U–Pb ages for Early Ordovician magmatism in central Spain. Journal of the Geological Society of London 157, 15–26.
Villaseca, C., Orejana, D., Belousova, E., Armstrong, R.A., Pérez-Soba, C., Jeffries, T.E., 2011. U–Pb isotopic ages and Hf isotope composition of zircons in Variscan gabbros from central Spain: evidence of variable crustal contamination. Mineralogy and Petrology 101, 151–167.
Walker, B.A., 2006. Geology and Geochronology of the Spirit Mountain Batholith, Southern Nevada: Implications for Timescales and Physical Processes of Batholith Construction. (Master Thesis) Vanderbilt University (78 pp.).
Wang, X., Griffin, W.L., Chen, J., Huang, P., Li, X., 2011. U and Th contents and Th/U ratios of zircon in felsic and mafic magmatic rocks: improved zircon-melt distribution coefficients. Acta Geologica Sinica 85, 164–174.

Watson, E.B., Harrison, T.M., 1983. Zircon saturation revisited—temperature and composition effects in a variety of crustal magma types. Earth and Planetary Science Letters 64, 295–304.
Whittington, A.G., Hofmeister, A.M., Nabelek, P.I., 2009. Temperature-dependent thermal diffusivity of the Earth's crust and implications for magmatism. Nature 458, 319–321.
Williams, I.S., 1998. U–Th–Pb geochronology by ion microprobe. In: McKibben, M.A., Shanks III, W.C., Ridley, W.I. (Eds.), Applications of Microanalytical Techniques to Understanding Mineralizing Processes: Reviews in Economic Geology, 7, pp. 1–35.
Williams, I.S., Claesson, S., 1987. Isotopic evidence for the Precambrian provenance and Caledonian metamorphism of high grade paragneisses from the Seve Nappes, Scandinavian Caledonides, II Ion microprobe zircon U–Th–Pb. Contributions to Mineralogy and Petrology 97, 205–217.
Yenes, M., Álvarez, F., Gutiérrez-Alonso, G., 1999. Granite emplacement in orogenic compressional conditions: the La Alberca–Béjar granitic area (Spanish Central System, Variscan Iberian Belt). Journal of Structural Geology 21, 1419–1440.
Zeck, H.P., Wingate, M.T.D., Pooley, G.D., 2007. Ion microprobe U–Pb zircon geochronology of a late tectonic granitic-gabbroic rock complex within the Hercynian Iberian belt. Geological Magazine 144, 157–177.